Autonomous Angles-Only Navigation for Spacecraft Swarms around Planetary Bodies

Justin Kruger
Department of Aeronautics and Astronautics
Stanford University
[redacted]

Kathryn Wallace
Department of Aeronautics and Astronautics
Stanford University
[redacted]

Adam W. Koenig
Department of Aeronautics and Astronautics
Stanford University
[redacted]

Simone D'Amico
Department of Aeronautics and Astronautics
Stanford University
[redacted]

Abstract*—This paper presents and demonstrates an algorithmic framework for autonomous navigation of spacecraft swarms around planetary bodies, using angles-only measurements from onboard cameras. Angles-only methods are compelling as they reduce reliance on external measurement sources. However, prior demonstrations have faced limitations, including 1) inability to treat more than one observer and target in a swarm, 2) lack of autonomy and reliance on external state information, and 3) treatment of only Earth-orbit scenarios. The new Absolute and Relative Trajectory Measurement System (ARTMS) overcomes these challenges and consists of three core modules leveraging novel algorithms: Image Processing, which tracks and identifies targets in images and computes their bearing angles; Batch Orbit Determination, which computes a swarm state initialization from angles-only measurements; and Sequential Orbit Determination, which uses an unscented Kalman filter to refine the swarm state estimate, seamlessly fusing measurements from multiple observers to achieve the autonomy, robustness and distribution needed for deep space navigation. Theoretical performance of ARTMS is investigated through a quantitative observability analysis of multi-observer angles-only navigation in Mars orbit. For swarms of at least 3 spacecraft and at least 2 observers, the complete swarm state is observable. After two orbits, the absolute orbit is estimated to within 1 km, target ranges are estimated to within 0.5%, and other relative state components are estimated to 0.02% of target range. Clock offsets are estimated to within 0.05s. These accuracies are validated with camera-in-the-loop simulations of a four-spacecraft swarm taking distributed measurements in an eccentric Mars orbit. ARTMS displays robust navigation across a variety of formations and under challenging conditions, and achieves the necessary performance to support the proposed objectives.

TABLE OF CONTENTS

978-1-7281-7436-5/21/$31.00

1. INTRODUCTION

DISTRIBUTED space systems and spacecraft swarms in particular can offer many advantages when compared to traditional monolithic spacecraft, including improved accuracy, coverage, flexibility, robustness, and the ability to achieve entirely new scientific objectives [1]. In recent years, this has been evidenced by a variety of Earth-orbiting missions such as GRACE (NASA), TanDEM-X (DLR) and MMS (NASA), which have employed multiple cooperative satellites with great success [2] [3] [4]. Subsequently, there has been strong interest in the application of distributed systems for space exploration and in deep space environments. Of special interest is the use of nanosatellite technology, with the aim of leveraging miniaturized hardware to achieve ambitious performance at reduced cost. Proposed deep space missions that demonstrate these aspects include the Autonomous Nanosatellite Swarming (ANS) mission concept, which aims to characterize an asteroid using a swarm of CubeSats [5], and the NASA Starling program, which has suggested applying CubeSat swarms for lunar exploration, communications and monitoring [6]. Proposed Earth-orbiting CubeSat swarm missions include the Space Weather Atmospheric Reconfigurable Multiscale Experiment (SWARM-EX), which will study the ionosphere and thermosphere [7], and the VIrtual Super Optics Reconfigurable Swarm (VISORS), which will implement a distributed solar telescope [8].

Nevertheless, the navigation of swarms in deep space presents significant technological challenges. Current swarm missions generally rely on Global Navigation Satellite System (GNSS) availability or frequent ground contacts for navigation. In contrast, swarms in deep space must aim to navigate with a high degree of autonomy, using only onboard resources. A promising solution in this regard is spaceborne angles-only navigation, in which observer satellites measure bearing angles to fellow swarm members via onboard Vision-Based Sensors (VBS). Cameras are passive, robust, low size-weight-power-cost sensors already present on the majority of spacecraft, conducive to both accurate navigation and swarm miniaturization. They also offer high dynamic range and are applicable to swarms operating at inter-spacecraft separations from several kilometers to several thousand kilometers. Figure 1 presents an example of a VBS image.

As documented in literature, two prior flight experiments have demonstrated angles-only navigation in orbit. In 2012, the Advanced Rendezvous using GPS and Optical Navigation (ARGON) experiment enabled the rendezvous of two smallsats in low Earth orbit (LEO) from inter-satellite sep-

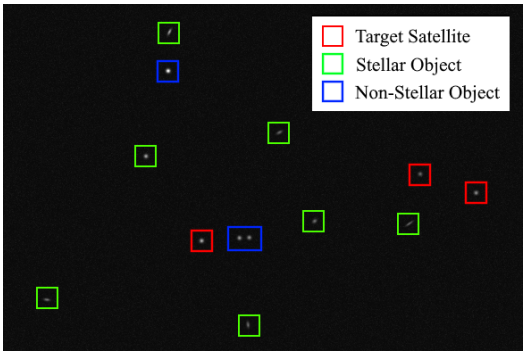

Figure 1. A synthetic space scene imaged by a a CubeSat star tracker, including classifications of visible point sources.

arations of 30km to 3km [9]. This was followed by the Autonomous Vision Approach Navigation and Target Identification (AVANTI) experiment in 2016, which similarly conducted a rendezvous of two smallsats from separations of 13km to 50m [10] [11]. While these demonstrations were successful, they are characterized by four key deficiencies that must be overcome to meet the needs of future swarm missions: 1) inability to accommodate multiple observers and multiple targets, 2) lack of autonomy and reliance on accurate a-priori relative orbit information, 3) reliance on external knowledge of the observer's absolute orbit, and 4) reliance on frequent translational maneuvers to resolve the weakly observable target range. There exists more sophisticated algorithms for individual navigation tasks such as target detection and tracking [12], initial relative orbit determination [13] [14], and sequential filtering [15], but these approaches suffer from a subset of the aforementioned limitations or are otherwise unsuitable for spaceborne angles-only navigation and its associated constraints. Such constraints include low measurement frequencies (e.g. minutes between images), frequent measurement gaps when spacecraft are in eclipse, limited onboard computational resources, and a need for high robustness for risk-averse flight applications.

To overcome these limitations and enable future swarm missions in deep space, Stanford's Space Rendezvous Laboratory (or SLAB) has proposed the Absolute and Relative Trajectory Measurement System (ARTMS) [16] [17]. ARTMS is a self-contained software payload that provides distributed, autonomous angles-only navigation for spacecraft swarms operating in any planetary orbit regime. It is divided into three modules based on angles-only algorithms recently developed at SLAB: image processing [18], batch orbit determination [19], and sequential orbit determination [16]. Each module operates with minimal a-priori information and applies absolute and relative state knowledge as it becomes available. ARTMS also exploits sharing of measurements over an inter-satellite link (ISL) to enable use of multiple observers for navigation. Overall, ARTMS provides orbit estimates for the host spacecraft and each target detected by its onboard VBS, as long as each swarm observer is provided with an estimate of its absolute orbit at a single epoch. The only hardware requirements posed on an observer by ARTMS are that it must possess a VBS and an ISL.

ARTMS will initially be flight tested in LEO by the Starling Formation-flying Optical eXperiment (StarFOX), which is part of the Starling technology demonstration mission under development at NASA Ames Research Center [6]. Its applicability to deep space has also been studied as part of a collaboration between SLAB and the NASA Jet Propulsion Laboratory. An example of a new mission concept enabled by ARTMS is a swarm of CubeSats taking distributed measurements of Mars' atmosphere, thermosphere, ionospheric plasmas, and transient magnetic fields. Such a swarm could be deployed from a primary spacecraft to enable greatly enhanced science return at minimal additional cost. Angles-only navigation can also be applied in secondary fashion – for instance, as a secondary navigation system for pairs of small satellites taking interferometric synthetic aperture radar (SAR) measurements of the Martian surface, or in the form of a swarm of CubeSats that provide an external orbit estimate for a larger, Mars-orbiting flagship spacecraft.

In light of these potential applications, this paper discusses the ARTMS architecture for autonomous, multi-observer angles-only navigation of spacecraft swarms around planetary bodies. Three primary contributions to the state of the art are presented. First, the ARTMS architecture and its algorithms are described, with a focus on the new capabilities necessary to enable deep space navigation and swarm mission concepts. This includes new multi-observer measurement assignment algorithms and estimation of clock offsets between swarm observers using angles-only measurements. Second, a quantitative observability analysis of multi-observer angles-only navigation in Mars orbit is presented, via computation of the estimated state covariance using a measurement noise matrix (representative of expected sensor performance) and a measurement sensitivity matrix across all measurement epochs. This analysis indicates that both absolute and relative swarm orbit determination can be achieved using inter-satellite angles-only measurements. Third, the estimation accuracies from the observability analysis are validated through simulations of angles-only navigation in Mars orbit using ARTMS. An example Mars swarm science mission is developed, enabled by purely angles-only navigation. Camera-in-the-loop simulations of representative navigation scenarios demonstrate sufficient navigation accuracy and robustness to achieve the stated science goals under challenging measurement conditions. ARTMS is therefore considered a promising solution for missions aiming to apply spacecraft swarms in deep space environments.

The paper is organised as follows. After this introduction, Section 2 presents mathematical background in regards to the swarm measurement model, dynamics model, and estimated state. Section 3 describes operational considerations for swarm navigation in deep space, with reference to potential mission applications. Section 4 introduces the ARTMS architecture and the algorithms necessary to enable robust, autonomous navigation in deep space. Section 5 presents the swarm observability analysis and relevant results. Section 6 details the simulated Mars mission and data generation pipeline, along with a discussion of results. Section 7 contains concluding remarks.

2. Modelling Preliminaries

Measurement Model

The ARTMS payload produces angles-only measurements by computing the time-tagged bearing angles to objects detected in VBS images. First, define the radial/along-track/cross-track (RTN) frame of the observer, denoted $\mathcal{R}$. It is centered on and rotates with the observer and consists of orthogonal basis vectors $\hat{\boldsymbol{x}}^{\mathcal{R}}$ (directed along the observer's absolute position vector); $\hat{\boldsymbol{z}}^{\mathcal{R}}$ (directed along the observer's orbital angular

momentum vector); and $\hat{\boldsymbol{y}}^{\mathcal{R}} = \hat{\boldsymbol{z}}^{\mathcal{R}} \times \hat{\boldsymbol{x}}^{\mathcal{R}}$ [20]. Similarly, define a frame $\mathcal{W}$ using $\hat{\boldsymbol{y}}^{\mathcal{W}}$ (directed along the observer's velocity vector); $\hat{\boldsymbol{z}}^{\mathcal{W}} = \hat{\boldsymbol{z}}^{\mathcal{R}}$; and $\hat{\boldsymbol{x}}^{\mathcal{W}} = \hat{\boldsymbol{y}}^{\mathcal{W}} \times \hat{\boldsymbol{z}}^{\mathcal{W}}$. $\mathcal{W}$ only differs from $\mathcal{R}$ by a rotation of the observer flight path angle ϕ_f about $\hat{\boldsymbol{z}}^{\mathcal{R}}$ with $\phi_f \approx 0$ in near-circular orbits [20].

Bearing angles consist of azimuth and elevation (α, ϵ) and subtend the line-of-sight vector $\delta\boldsymbol{r}^{\mathcal{V}} = (\delta r_x^{\mathcal{V}}, \delta r_y^{\mathcal{V}}, \delta r_z^{\mathcal{V}})$ from the observer to the target. Superscript $\mathcal{V}$ indicates description in the observer VBS coordinate frame, consisting of orthogonal basis vectors $\hat{\boldsymbol{x}}^{\mathcal{V}}, \hat{\boldsymbol{y}}^{\mathcal{V}}, \hat{\boldsymbol{z}}^{\mathcal{V}}$. Without loss of generality, this paper assumes a camera with boresight $\hat{\boldsymbol{z}}^{\mathcal{V}}$ aligned with $\pm\hat{\boldsymbol{y}}^{\mathcal{W}}$ (as appropriate), $\hat{\boldsymbol{y}}^{\mathcal{V}}$ aligned with $\hat{\boldsymbol{z}}^{\mathcal{W}}$, and $\hat{\boldsymbol{z}}^{\mathcal{V}} = \hat{\boldsymbol{x}}^{\mathcal{V}} \times \hat{\boldsymbol{y}}^{\mathcal{V}}$. Bearing angles are then computed via [21]

$$\begin{pmatrix} \alpha \\ \epsilon \end{pmatrix}^{\mathcal{V}} = \begin{pmatrix} \arcsin \delta r_y^{\mathcal{V}} / ||\delta\boldsymbol{r}^{\mathcal{V}}||_2 \\ \arctan \delta r_x^{\mathcal{V}} / \delta r_z^{\mathcal{V}} \end{pmatrix} \tag{1}$$

Bearing angles can be related to the inertial frame by rotating $\delta\boldsymbol{r}^{\mathcal{V}}$ into the Planet-Centered Inertial (PCI) frame $\mathcal{P}$, as per

$$\delta\boldsymbol{r}^{\mathcal{P}} = {}^{\mathcal{V}}\overrightarrow{\boldsymbol{R}}^{\mathcal{P}} \delta\boldsymbol{r}^{\mathcal{V}} \tag{2}$$

where ${}^{\mathcal{V}}\overrightarrow{\boldsymbol{R}}^{\mathcal{P}}$ denotes a rotation from frame $\mathcal{V}$ into frame $\mathcal{P}$. This rotation matrix is computed by performing attitude determination using stars identified by the VBS [9]. Rotation matrices ${}^{\mathcal{R}}\overrightarrow{\boldsymbol{R}}^{\mathcal{P}}$ and ${}^{\mathcal{W}}\overrightarrow{\boldsymbol{R}}^{\mathcal{P}}$ can be computed using the observer's absolute orbit estimate. Figure 2 depicts the relationship between coordinate frames and bearing angles.

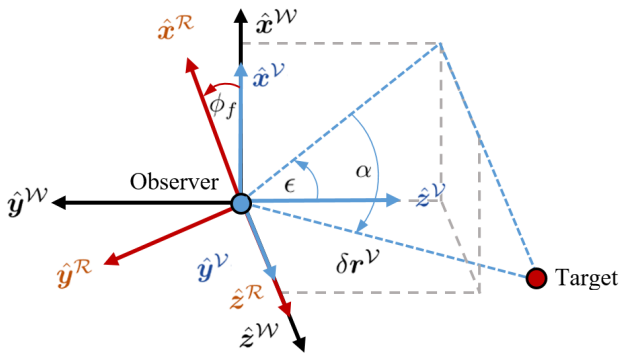

Figure 2. Definition of the target line-of-sight vector and bearing angles with respect to $\mathcal{V}, \mathcal{R}$ and $\mathcal{W}$. Here, the VBS points in the anti-velocity direction.

State Parametrization

ARTMS represents the absolute state $\boldsymbol{\alpha}$ of the observer in terms of quasi-nonsingular orbit elements (OE), with

$$\boldsymbol{\alpha} = \begin{pmatrix} a \\ e_x \\ e_y \\ i \\ \Omega \\ u \end{pmatrix} = \begin{pmatrix} a \\ e\cos\omega \\ e\sin\omega \\ i \\ \Omega \\ \omega + M \end{pmatrix} \tag{3}$$

Above, a, e, i, Ω, ω and M are the canonical Keplerian OE of semi-major axis, eccentricity, inclination, right ascension of the ascending node, argument of periapsis, and mean anomaly respectively, and u is the mean argument of latitude. All are computed with respect to $\mathcal{P}$. Fully nonsingular OE have also been defined for equatorial orbits [20].

The relative orbit $\delta\boldsymbol{\alpha}$ of a target spacecraft, as tracked by an observer, is described by the quasi-nonsingular relative orbit elements (ROE) [22]. The ROE state parametrization is defined in terms of the absolute OE of the observer and target (denoted by subscripts 'o' and 't' respectively) via

$$\delta\boldsymbol{\alpha} = \begin{pmatrix} \delta a \\ \delta\lambda \\ \delta e_x \\ \delta e_y \\ \delta i_x \\ \delta i_y \end{pmatrix} = \begin{pmatrix} (a_t - a_o)/a_o \\ (u_t - u_o) + (\Omega_t - \Omega_o)\cos i_o \\ e_{x,t} - e_{x,o} \\ e_{y,t} - e_{y,o} \\ i_t - i_o \\ (\Omega_t - \Omega_o)\sin i_o \end{pmatrix} \tag{4}$$

Above, δa is the relative semi-major axis, $\delta\lambda$ is the relative mean longitude, $\delta\boldsymbol{e} = (\delta e_x, \delta e_y)$ is the relative eccentricity vector with magnitude δe and phase ϕ, and $\delta\boldsymbol{i} = (\delta i_x, \delta i_y)$ is the relative inclination vector with magnitude δi and phase θ. Fully nonsingular ROE have also been defined for equatorial orbits [23].

The ARTMS state also includes several optional components. First are absolute empirical accelerations for the observer and differential empirical accelerations for targets, defined as

$$\boldsymbol{a}_{\text{emp}}^{\mathcal{R}} = \begin{pmatrix} a_x \\ a_y \\ a_z \end{pmatrix}^{\mathcal{R}} \tag{5}$$

$$\delta\boldsymbol{a}_{\text{emp}}^{\mathcal{R}} = \begin{pmatrix} \delta a_x \\ \delta a_y \\ \delta a_z \end{pmatrix}^{\mathcal{R}} = \begin{pmatrix} a_{x,t} - a_{x,o} \\ a_{y,t} - a_{y,o} \\ a_{z,t} - a_{z,o} \end{pmatrix}^{\mathcal{R}} \tag{6}$$

respectively in $\mathcal{R}$. Empirical accelerations are used to approximately capture unmodeled dynamics, and are more computationally efficient than numerically integrating the full differential equations of relative motion [21]. Other optional state components are the absolute clock errors and clock drift rates of the observer, and differential clock offsets and clock drift rates of targets with respect to the observer, defined as

$$\boldsymbol{c}_{\text{err}} = \begin{pmatrix} c_{\text{err}} \\ d_{\text{err}} \end{pmatrix} \tag{7}$$

$$\delta\boldsymbol{c}_{\text{err}} = \begin{pmatrix} \delta c_{\text{err}} \\ \delta d_{\text{err}} \end{pmatrix} = \begin{pmatrix} c_{\text{err},t} - c_{\text{err},o} \\ d_{\text{err},t} - d_{\text{err},o} \end{pmatrix} \tag{8}$$

Above, c_{err} is a clock offset and d_{err} is a clock drift rate. For n detected targets, the complete ARTMS state is therefore

$$\boldsymbol{x} = (\boldsymbol{\alpha}, \boldsymbol{a}, \boldsymbol{c}, \delta\boldsymbol{\alpha}_1, \delta\boldsymbol{a}_1, \delta\boldsymbol{c}_1, ..., \delta\boldsymbol{\alpha}_n, \delta\boldsymbol{a}_n, \delta\boldsymbol{c}_n) \tag{9}$$

Additional state components – such as VBS sensor biases or spacecraft ballistic properties – can also be estimated by ARTMS [16] but are not included here.

Dynamics Model

ARTMS propagates the absolute orbits of observer and target spacecraft using numerical integration of the Gauss Variational Equations (GVE). For state $\boldsymbol{\alpha}$, the osculating OE of each spacecraft evolve according to

$$\dot{\boldsymbol{\alpha}} = G(\boldsymbol{\alpha})\boldsymbol{d}^{\mathcal{R}} \tag{10}$$

where $G \in \mathbf{R}^{6\times3}$ is the well-documented GVE state transition matrix [24] and $\boldsymbol{d}^{\mathcal{R}}$ is the perturbing acceleration expressed in $\mathcal{R}$. Depending on the orbit regime, common perturbations are spherical harmonic gravity, atmospheric drag,

third-body gravity and solar radiation pressure. Analytic dynamics models for the mean OE which include the effects of J_2 and J_3 gravity perturbations are alternately used when computational efficiency is paramount. J_2 causes secular drifts in M, ω and Ω [25] while J_3 causes long-periodic changes in e, i, ω and Ω [26]. Analytic models including common perturbations are also available for ROE [23] [27].

A particularly useful aspect of ROE is that they provide geometric intuition regarding target relative motion. As shown in [22] for near-circular orbits, there is a linear map between the ROE and the target's curvilinear position vector $\delta\boldsymbol{r}$ in the observer's RTN frame

$$\delta\boldsymbol{r} = \begin{bmatrix} \delta r_R \\ \delta r_T \\ \delta r_N \end{bmatrix} \approx a_o \begin{bmatrix} \delta a - \delta e\ \cos(u_o - \phi) \\ \delta\lambda + 2\delta e\ \sin(u_o - \phi) \\ \delta i\ \sin(u_o - \theta) \end{bmatrix} \tag{11}$$

The near-circular case was extended to eccentric orbits [21] by defining the eccentric ROE $\delta\boldsymbol{\alpha}^* = (\delta a, \delta\lambda^*, \delta e_x^*, \delta e_y^*, \delta i_x, \delta i_y)$. The eccentric ROE revert to traditional ROE for $e_o \approx 0$. The resulting map is

$$\delta\boldsymbol{r} \approx r_o \begin{bmatrix} \delta a - \frac{e_o}{2}\delta e_x^* - \delta e^* \left(\cos(f_o - \phi^*) + \frac{e_o}{2}\cos(2f_o - \phi^*)\right) \\ \delta\lambda^* + \delta e^* \left(2\sin(f_o - \phi^*) + \frac{e_o}{2}\sin(2f_o - \phi^*)\right) \\ \delta i \sin(f_o + \omega_o - \theta) \end{bmatrix} \tag{12}$$

Figure 3 presents relative motion in RTN for small separations. Oscillatory motion produced by target relative orbits is shown in black, possessing the same frequency as the orbit. Oscillatory motion produced by orbit eccentricity is shown in red, acting at twice the frequency of the orbit. δa and $\delta\lambda^*$ capture mean offsets in the radial and along-track directions respectively; magnitudes of δe^* and δi correspond to magnitudes of oscillations in the RT and RN planes respectively; and phases of δe^* and δi dictate the orientation and aspect ratio of the tilted ellipse in the RN plane. The eccentricity of the observer's orbit superimposes additional offsets and higher-frequency oscillations in the RT and RN planes.

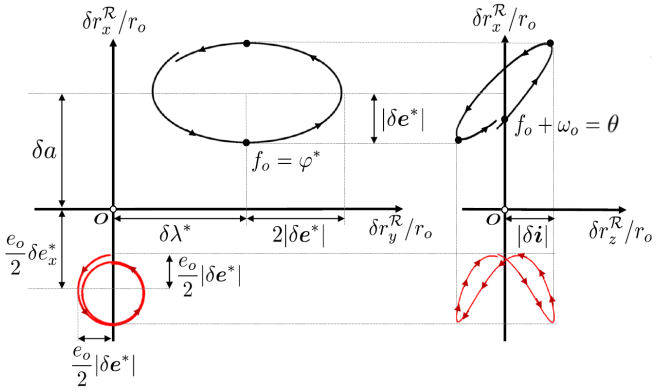

Figure 3. Target relative motion in the $\hat{\boldsymbol{x}}^{\mathcal{R}}$-$\hat{\boldsymbol{y}}^{\mathcal{R}}$ (RT) and $\hat{\boldsymbol{x}}^{\mathcal{R}}$-$\hat{\boldsymbol{z}}^{\mathcal{R}}$ (RN) planes. Motion that is first-order in spacecraft separation is in black. Contributions proportional to e are in red [16].

Clock offsets are propagated within ARTMS using a simple model defined by

$$\dot{\boldsymbol{c}}_{\text{err}} = \begin{bmatrix} 0 & T_s \\ 0 & 0 \end{bmatrix} \boldsymbol{c}_{\text{err}} \tag{13}$$

where T_s is the propagation timestep.

3. Operational Considerations

In comparison to prior angles-only architectures focusing on single observers and targets, the extension to spacecraft swarms requires new capabilities – as does the extension from Earth orbit to deep space. When introducing ARTMS, it is thus useful to consider the types of multi-satellite mission which are enabled by angles-only navigation and the resulting operational constraints or requirements that must be met.

Consider angles-only as the primary navigation method for a swarm science mission, taking cooperative, distributed or repeating measurements at varying scales impossible with a single spacecraft. Example objectives include solar wind measurements [6] or characterization of planetary atmospheres [7]. Pure angles-only navigation may not be sufficient for objectives requiring extremely accurate position knowledge, such as planetary interferometric SAR mapping [3]. However, it can still be used to support the mission in a secondary fashion, such as during low power modes or formation acquisition. Furthermore, angles-only techniques can be leveraged to support a larger, flagship spacecraft via 'navigation buddies', i.e. a swarm of small satellites deployed from the flagship to provide real-time absolute orbit determination in a cooperative manner. This swarm could even carry science instruments itself. More ambitious scales can also be explored. Consider a planetary navigation service, in which a constellation of small satellites broadcasts its positions as autonomously determined on-board using angles-only navigation. This information can then be used for position triangulation by other ground-based or orbiting assets. Such a system could be used to support future Mars exploration efforts with lower costs (but also lower accuracy) than a traditional GNSS system.

In view of these examples, there are three broad operational capabilities the angles-only system must possess. First is distribution, in that the architecture should be capable of navigation for arbitrary numbers of swarm observers and targets, and take advantage of distributed or decentralized operation to improve overall reliability, flexibility and scalability. This relates to a primary driver behind the adoption of swarm-based concepts and spacecraft miniaturization, i.e. the potential for groups of small satellites to achieve enhanced capabilities at lower cost and on faster timelines [1]. Thus, the architecture should also rely on hardware suitable for small satellites or nanosatellites in regards to sensing, communications bandwidth, and processing power. This is supported by the use of VBS, which are cheap, low mass, low power systems. In comparison, the efficacy of (for example) inter-satellite ranging is potentially limited for nanosatellites.

Second, there is a preference for autonomy and navigation using only onboard sensors and resources. Traditionally, deep space navigation has relied on external frameworks such as the NASA Deep Space Network (DSN). However, the increasing number of interplanetary spacecraft has placed strain on these capabilities – strict scheduling is already necessary to ensure timely DSN navigation solutions [28]. If in future, individual swarm members require DSN contact, navigation rapidly becomes inefficient or untenable. Swarm navigation methods should therefore require minimal ground contact in the sense of being self-initializing and self-sustaining. Existing angles-only architectures have not achieved this, requiring accurate a-priori relative orbit information for navigation initialization and regular external absolute orbit updates to maintain state convergence [9] [10] [16]. Furthermore, if ground updates are sparse, it becomes necessary to estimate additional state components such as the clock errors of swarm

observers, which is untreated by prior work in this field.

Third, navigation must guarantee high robustness, especially for interplanetary missions incurring significant investment. From a hardware perspective, VBS solutions are again attractive because cameras are simple, passive, robust and accurate. However, robustness of estimation is challenging. Prior work has shown that bearing angle measurements from a single observer do not distinguish between a change in the mean argument of latitude (u) of the observer and the relative mean longitude ($\delta\lambda$) of a target, creating an unobservable mode and gradual state divergence [19]. Furthermore, such methods have displayed weak observability because bearing angles do not contain explicit target range information [29] [30]. It has been suggested to use translational maneuvers to disambiguate target range, but this limits mission lifetime from associated propellant use and increases complexity by requiring maneuver plans. More broadly, navigation should also be robust to errors in the state estimate or a-priori information, and agnostic to swarm orbit geometries and the specific planetary dynamic environment.

4. ARTMS ARCHITECTURE

In response to these considerations, a novel navigation architecture has been developed by Stanford's SLAB. "ARTMS" is a self-contained software payload that provides autonomous, distributed angles-only navigation for spacecraft swarms in planetary orbit regimes [16] [17]. To describe its structure, the following terminologies are adopted. The "observer" refers to the spacecraft hosting the instance of ARTMS being discussed. A "remote observer" is another spacecraft hosting an ARTMS payload that is providing measurements over the ISL. The "swarm" consists of all observers and all other relevant "targets", which are space objects tracked by the observers. Observers might only track a subset of the swarm and often, the targets tracked by an observer will include one or more remote observers. Figure 4 presents an example.

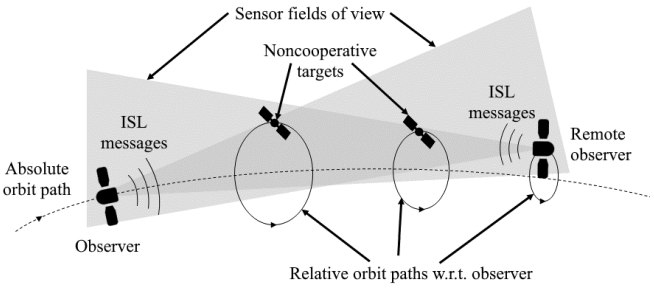

Figure 4. Illustration of ARTMS observers and targets.

A high-level overview of ARTMS is shown in Figure 5. It consists of of three core software modules: IMage Processing (IMP), Batch Orbit Determination (BOD) and Sequential Orbit Determination (SOD). Data sources are the VBS, which provides time-tagged images to ARTMS; the ISL, which communicates orbit estimates and bearing angle measurements between all swarm observers; the spacecraft bus, which provides additional attitude information; and the ground segment, which provides telecommands and receives telemetry from ARTMS instances. In this paper, it is assumed GNSS measurements are unavailable.

Operation of each module is briefly described as follows. First, the IMP module uses images from the VBS to produce batches of bearing angle measurements with corresponding uncertainties for all detected targets in the field of view (FOV). The only prior information needed by IMP is a coarse estimate of the observer's absolute orbit at a single epoch, provided by a source such as the DSN. IMP measurement batches are provided to BOD and SOD. The BOD module uses the IMP angle batches, as well as the aforementioned estimate of the observer's orbit, to compute state estimates for all spacecraft in the local swarm (including itself and all targets observed by the VBS). This state estimate is provided to the SOD module for initialization and fault detection. The SOD module uses the BOD state estimate to initialize an unscented Kalman filter (UKF), which fuses measurements from IMP and remote ISL observers to refine the orbit estimates of all spacecraft in the local swarm (as well as auxiliary parameters such as ballistic coefficients or differential clock offsets). State updates from known maneuvers are applied if necessary. SOD then provides updated state estimates to IMP to more efficiently assign bearing angles in new images to existing targets. The orbit estimate and bearing angles are also sent to the ISL. Sample times are on the order of minutes for IMP and the VBS (dependent on orbit period, to provide approximately 50-100 measurements per orbit), once per orbit for BOD, and one minute for SOD.

Algorithms are scalable to arbitrary numbers of observers and targets, and navigation is distributed between observers via sharing of measurements and state estimates over the ISL. The three modules also operate with essentially no support from ground-based resources. As described in the following sections in more detail, IMP applies novel data association algorithms, in concert with BOD estimation algorithms, to self-initialize navigation using a single external absolute orbit measurement per observer. Modules subsequently take advantage of additional information as it becomes available to enable near-total autonomy. Of particular importance, with respect to prior work, is the application of multiple observers. SOD employs new algorithms to match measurements from different observers to corresponding targets, and the resulting stereo measurements greatly improve state estimate robustness, convergence and accuracy. Unobservable modes are removed and it becomes easier to disambiguate target range. ARTMS is then able to estimate the swarm's absolute and relative orbits with exclusively bearing angles, eliminating reliance on maneuvers and external measurement sources. Detailed descriptions of IMP, BOD and SOD algorithms are also available in [18], [19] and [16] respectively.

Image Processing

The objective of IMP is to produce batches of time-tagged bearing angle measurements to each target using a coarse estimate of the observer's orbit and images provided by the onboard VBS. This is accomplished in two phases. First, each incoming image is processed and reduced to a set of inertial bearing angles that may correspond to resident space objects. Second, these candidate bearing angles are used to track known targets and detect new targets using an approach inspired by multi-hypothesis tracking (MHT) [12].

The first phase of IMP uses a set of well-known algorithms. First, a centroiding algorithm is used to simplify the raw image into a list of pixel cluster centroids [31]. Second, these centroids are converted to unit vectors in the sensor frame using the calibrated sensor model. Next, the pyramid star identification algorithm [32] is applied to remove stellar objects (SO) from the list of pointing vectors. Uncatalogued SO are detected by considering objects with unchanging inertial unit vectors between images. Similarly, camera hotspots are removed by considering objects with unchanging pixel

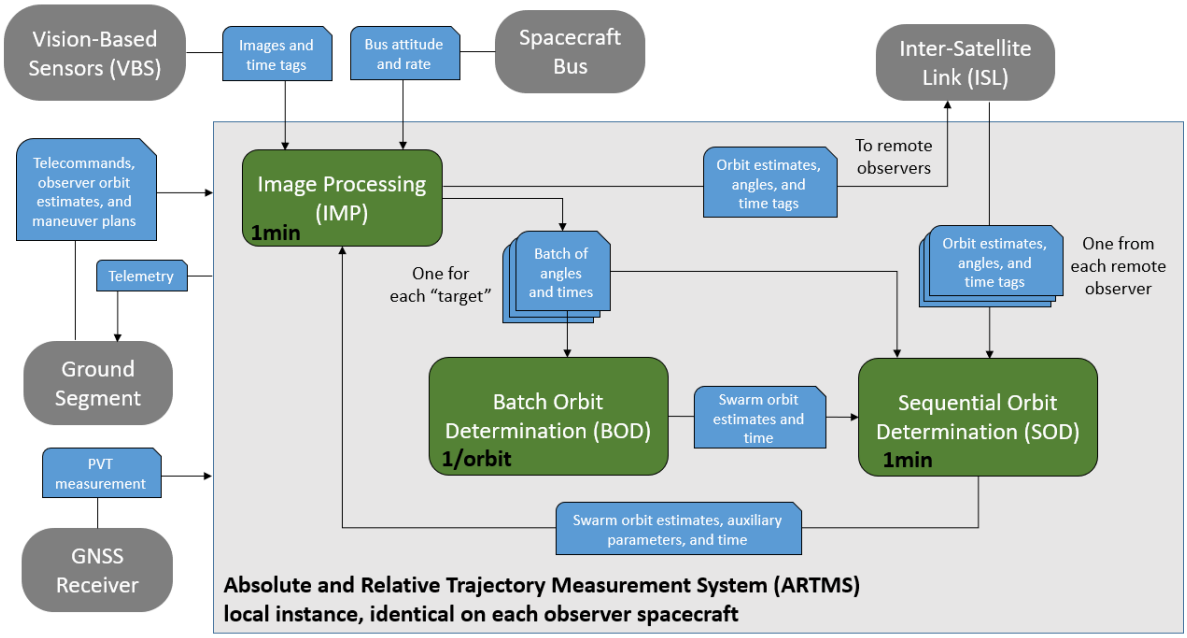

Figure 5. Architecture of the ARTMS payload including external systems/data sources (dark gray), software modules (green), and exchanged data (blue). The GNSS inputs (when available) and ground inputs are are provided to all modules; the telemetry output consists of all modules' data outputs.

coordinates. The VBS attitude is computed from the pointing vectors to identified stars in the inertial and sensor frames using the q-method [33]. The remaining minimal set of inertial unit vectors likely corresponds to known targets or other unknown objects in the FOV.

In the second phase, measurements must be assigned to targets currently being tracked or used to initialize new targets, without requiring a-priori relative orbit knowledge. To accomplish this, IMP employs the new Spacecraft Angles-only MUltitarget tracking System (SAMUS) algorithm [18], which has two key requirements: 1) a coarse estimate of the observer's absolute orbit is provided, and 2) targets do not perform large translational maneuvers during the tracking period. SAMUS has been designed to meet the constraints of angles-only navigation in space, i.e. to achieve close to 100% measurement assignment precision with low measurement frequencies and limited computational resources. It applies the core concept of MHT in that as measurements arrive, several simultaneous hypotheses are maintained for their association into target tracks. The algorithm converges towards the correct hypothesis over time. MHT is chosen as a basis because it is mature and demonstrably accurate, with its primary disadvantage being the need to frequently and heuristically trim hypotheses for real-time computation [34]. To overcome this, SAMUS applies domain-specific knowledge to develop precise trimming criteria.

These criteria stem from Equation 12, which defines a mapping between the target's curvilinear position vector in RTN and its eccentric ROE. In this mapping, note that true anomaly f_o is the only quickly-varying term. Other terms, as defined by the OE and ROE, vary slowly in the presence of perturbations such as spherical harmonic gravity and atmospheric drag [22]. In most angles-only scenarios of interest, swarm members are in relatively close proximity in inertial space and are affected similarly by perturbations. By synchronously differencing the measured unit vectors of different targets in RTN – in essence, using one target's track as a virtual, moving origin for another – perturbation effects are approximately cancelled between targets. After this transformation, all terms in the model of Equation 12 other than f_o can be considered constant on the timescale of image-to-image tracking. Thus, target motion is periodic with known form and parameter f_o. Even if specific ROE are unknown, this expectation can be leveraged to assess hypotheses.

First, the Equation 12 model can be fitted to measurement tracks, and used to assess goodness of fit and predict upcoming measurements. Given $i = 1, ..., n$ past bearing angles in a track, Equation 12 can be rearranged into a pair of separable linear systems in azimuth and elevation, via [18]

$$\begin{bmatrix} x_{1,1} & x_{1,2} & x_{1,3} \\ \vdots & \vdots & \vdots \\ x_{n,1} & x_{n,2} & x_{n,3} \end{bmatrix} \begin{bmatrix} y_1 \\ y_2 \\ y_3 \end{bmatrix} = \begin{bmatrix} \epsilon_1 \\ \vdots \\ \epsilon_n \end{bmatrix} \tag{14}$$

$$\begin{bmatrix} x_{1,4} & x_{1,5} & x_{1,6} \\ \vdots & \vdots & \vdots \\ x_{n,4} & x_{n,5} & x_{n,6} \end{bmatrix} \begin{bmatrix} y_4 \\ y_5 \\ y_6 \end{bmatrix} = \begin{bmatrix} \alpha_1 \\ \vdots \\ \alpha_n \end{bmatrix} \tag{15}$$

The $x_{i,j}$ values are computed using the one-off observer absolute orbit estimate, propagated into each measurement epoch using the analytic ARTMS dynamics model. The unknown y_j terms are scaled ROE equivalents in bearing angle space and can be solved for via least squares as long as at least three past measurements exist. Subsequently, upcoming measurements in a new image can be predicted.

Second, a set of kinematic rules can be derived from Equation 12 to assess which hypotheses are physically reasonable. Only tracks which pass all rules are propagated. Briefly, the rules are summarised as:

1. Track velocities must be below a set maximum

2. Track velocities must be consistent over time
3. Tracks should generally not feature acute angles
4. Tracks should turn in a consistent direction
5. New data must be close to the predicted measurement

Their application increases efficiency of MHT by preventing formation of unlikely tracks. Mathematical definitions for these rules are provided in [18]. When multiple tracks pass all rules, SAMUS scores propagated tracks via ten criteria, which assess how well each track fulfils the expectations of Equation 12 and prior motion. In contrast to traditional MHT methods – which often rely on a single Mahalanobis distance metric for scoring, or probabilistic estimates – SAMUS aims to be more robust and definitive. Often, target tracks intersect or are in proximity in the image plane, or motion between images is on the order of VBS noise, and a single metric may temporarily support an incorrect hypothesis. By using a larger set, consensus supports the correct choice over time.

To initialize new tracks, SAMUS employs the Density-Based Spatial Clustering of Applications with Noise (DBSCAN) algorithm [35]. DBSCAN clusters require $\geq n_D$ points within small radius ϵ_D. Because targets are in similar orbits to observers, their velocities compared to other objects in the FOV are low [10]. Previously untracked targets are initialized by applying DBSCAN to the set of unidentified measurements from the past several images, and applying the SAMUS kinematic rules to found clusters. Finally, given the use of visual measurements, tracking is often interrupted by orbit eclipse periods. To connect shorter tracks on either side of an eclipse, the fit of Equation 14 – 15 is computed for every possible pair of tracks. The combination of compatible pairs which produces the least fitting residuals is chosen. Figure 6 presents an overview of core SAMUS operations.

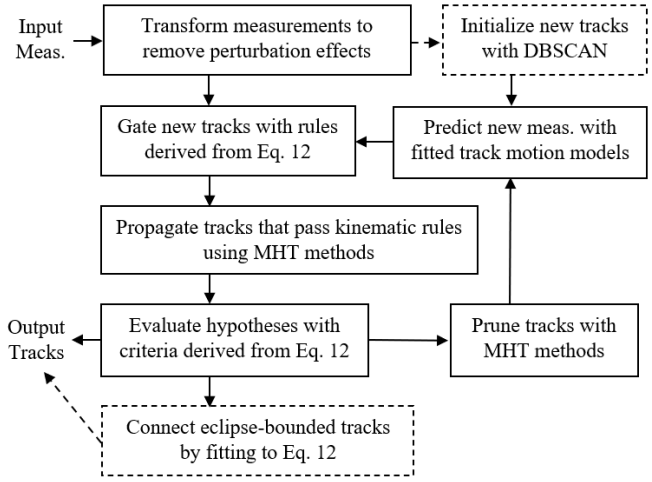

Figure 6. SAMUS algorithm summary and core sequence of operations. Dashed lines denote steps that only occur at relevant epochs.

SAMUS is also able to cooperate with SOD and apply target state knowledge, if available. SOD state estimates are propagated into the current epoch, and an unscented transform is used to compute target measurements and associated covariance regions. The kinematic rules are replaced by a validity region based on this predicted measurement and covariance, and the Mahalanobis distance between predicted and assigned measurement is employed for track scoring. In this mode, maneuvering targets can be tracked by IMP.

Batch Orbit Determination

The BOD module must produce orbit estimates for the swarm with sufficient accuracy to initialize the SOD module, using only a single coarse estimate of the observer orbit and batches of bearing angles to each target from the onboard sensor. Typical measurement collection periods are 1-2 orbits. State estimation is accomplished using a new algorithm [19] that sequentially estimates the relative orbits of each target while simultaneously refining the estimate of the semimajor axis of the observer's orbit. The analytic dynamics models from Section 2 are employed to minimize computation cost. Note that the perturbations which must be included in the model depend on the planetary environment. For example, in LEO, the J_2 oblateness perturbation is generally dominant. However, in low Mars orbit, the J_3 perturbation has comparatively more influence [36] and must also be included.

For each target, BOD state estimation is a four-step procedure as inspired by [14]. First, a 1-D family of state estimates is computed for specified samples of $\delta\lambda$, using iterative batch least squares refinement until either 1) a specified iteration limit is reached, or 2) the step size is smaller than a specified convergence threshold. Second, the final state estimate is selected as the one which produced the least measurement residuals. A typical choice of $\delta\lambda$ is to sample the expected state space in 1km intervals. A conceptual illustration of BOD state selection for a single target is shown in Figure 7.

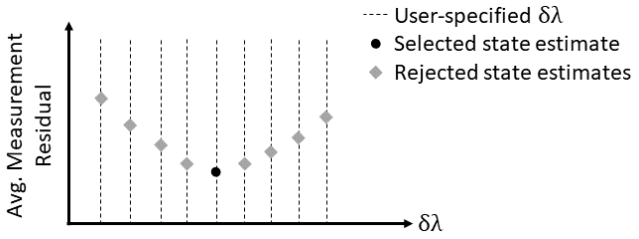

Figure 7. Conceptual illustration of converged measurement residuals for rejected (gray) and selected (black) state estimates for specified $\delta\lambda$ values in BOD.

Third, the measurement noise matrix for each measurement (denoted $\boldsymbol{R}_{\text{vbs}}$) is estimated using the measurement residuals corresponding to the final state estimate. Fourth, the covariance for estimated state components $\boldsymbol{P}_{\text{est}}$ is computed, via

$$\boldsymbol{P}_{\text{est}} = \boldsymbol{Y}^*_{\text{est}}(N\boldsymbol{R}_{\text{vbs}} + \boldsymbol{Y}_{\text{prior}}\boldsymbol{P}_{\text{prior}}\boldsymbol{Y}^T_{\text{prior}})\boldsymbol{Y}^{*T}_{\text{est}} \qquad (16)$$

where $\boldsymbol{Y}^*_{\text{est}}$ is the pseudoinverse of the measurement sensitivity matrix for estimated state components, $\boldsymbol{Y}_{\text{prior}}$ is the measurement sensitivity matrix for a-priori information (e.g. orbit elements other than the semimajor axis), $\boldsymbol{P}_{\text{prior}}$ is the uncertainty of a-priori information, and N is the number of bearing angle measurements. This formulation allows BOD to seamlessly transition between domains where uncertainty is driven by sensor performance or by errors in the a-priori information. Finally, the ROE estimates for each target are appended to the refined estimate of the observer's absolute orbit, forming a complete local swarm state estimate.

It was demonstrated in [19] that this approach can provide relative orbit estimates with target range errors of less than 20% (3-σ) in the presence of absolute orbit errors of up to 2 km using only two orbits of bearing angle measurements across a wide range of Earth orbit regimes. Additionally, the computation time required to estimate the state of each

target with two orbits of measurements is approximately five seconds on a desktop PC with a 3.5GHz processor. Computation cost increases linearly with the number of targets in the local swarm, allowing the algorithm to efficiently scale to large swarms.

Sequential Orbit Determination

The SOD module continually refines orbit estimates of the observer and its targets − and auxiliary parameter estimates such as sensor biases, ballistic coefficients, and differential clock offsets − by seamlessly fusing measurements from all observers transmitted over the ISL. SOD applies the bearing angle measurement model and numerical GVE dynamics model from Section 2 within a UKF framework, which preserves higher order moments in the probability distribution to enable maneuver-free convergence using angles-only measurements from a single observer [16]. Three additional features are included in the SOD module to to maximize performance. First, adaptive process noise estimation is used to improve convergence speed and robustness to errors in the dynamics model [37]. Second, the state definition is organized in a way that exploits the structure of the Cholesky factorization to reduce the number of calls to the orbit propagator by almost a factor of two [38]. Third, measurements from remote observers are assigned to locally-tracked targets using selection criteria based on the Mahalanobis distances between the estimated bearing angles to each target and each candidate measurement.

To enable remote observer measurement assignment, it is first necessary to know whether any locally-tracked targets are remote observers. Let σ_{mn} denote the Mahalanobis distance between the broadcast orbit estimate of remote observer m and the orbit estimate of local target n. Remote observer m is identified as target n if four conditions are fulfilled:

1. m has not yet been identified
2. $\sigma_{mn} \leq \epsilon_{\text{id}}$: remote observer m's orbit is similar to the estimate of the target n's orbit.
3. $\sigma_{pn} \geq \epsilon_{\text{safe}}\ \forall\ p \neq m$: there is no other remote observer that fits target n's orbit.
4. $\sigma_{mq} \geq \epsilon_{\text{safe}}\ \forall\ q \neq n$: there is no other target that fits remote observer m's orbit.

Identifications are kept until $\sigma_{mn} \geq \epsilon_{\text{remove}}$. Parameters are user-specified with $\epsilon_{\text{remove}} > \epsilon_{\text{safe}} > \epsilon_{id} > 0$. Formal target identification ensures that measurements by observer m can never be considered as measurements of observer m − preventing this contradiction improves robustness and reduces the search space when assigning measurements.

Next, measurements from remote observer must be assigned to targets of the local observer. Let σ_{ij} denote the Mahalanobis distance between measurement i from the remote observer and the estimated measurement of local target j. Measurement i from the remote observer is assigned to local target j if three conditions are satisfied:

1. $\sigma_{ij} \leq \epsilon_{\text{assign}}$: remote measurement i is close to the modeled measurement of local target j.
2. $\sigma_{kj} \geq \epsilon_{\text{ambig}}\ \forall k \neq i$: no other candidate measurement fits the estimated state of target j.
3. $\sigma_{il} \geq \epsilon_{\text{ambig}}\ \forall l \neq j$: no other local target fits remote measurement i.

The ϵ parameters are user-specified with with $\epsilon_{\text{ambig}} > \epsilon_{\text{assign}} > 0$. Figure 8 illustrates four possible cases of modeled and observed measurements from a remote observer which (from left to right) show all conditions satisfied and violations of Condition 1, Condition 2, and Condition 3, respectively. Together, these conditions ensure that measurements are only assigned when the observed and modeled measurements uniquely agree with a statistical certainty determined by the values of ϵ_{assign} and ϵ_{ambig}. The values of these parameters should be selected based on the expected number of targets, relative motion geometry, sensor noise, and available orbit knowledge for general swarming missions. However, for the scenarios in this paper, the authors have found that setting $\epsilon_{\text{id}} = 3, \epsilon_{\text{safe}} = 6, \epsilon_{\text{remove}} = 10, \epsilon_{\text{assign}} = 3$ and $\epsilon_{\text{ambig}} = 6$ provide robust multi-observer identification.

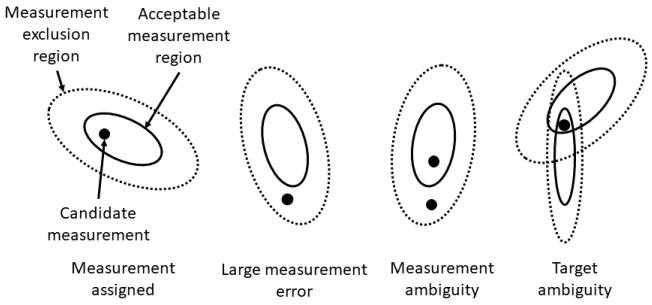

Figure 8. Illustration of conditions in which all measurement criteria are satisfied (left) and conditions that violate each of the measurement assignment criteria (right).

State Parametrization

The choice of ARTMS state parametrization, as defined in Section 2, also provides crucial advantages. Firstly, use of ROE to represent target states means that the weakly observable range to each target is primarily captured by the $\delta\lambda$ term in most relative motion geometries, with other ROE being strongly observable [39]. This allows ARTMS to maximize accuracy by applying separate state estimation techniques to different components, as is done for BOD. Second, the UKF in SOD is able to incorporate nonlinearities in the dynamics and measurement models in an efficient and accurate manner, which is leveraged to completely estimate observer and target states without maneuvers. Third, OE and ROE states vary slowly with time, which enables accurate numerical integration using Gauss's variational equations with large timesteps [40] for efficient onboard orbit propagation. Similarly, several accurate analytical dynamics models for ROE have been developed for Earth orbit [23] [27] that can be adapted to other planetary regimes.

Inclusion of the differential clock offsets and clock drift rates between swarm observers in the estimated state further aids robustness and minimizes necessary ground contact. If clock offsets are not updated regularly, there will be measurement errors due to mismatches between the epochs of ISL measurements and the local ARTMS instance. This most prominently manifests as steady-state bias in $\delta\lambda$: a remote measurement being late or early is similar to the inter-satellite range appearing smaller or larger. Divergence in the absolute orbit estimate is also displayed as observer clocks drift. During target identification, measurement assignment, and UKF measurement updates, clock offsets are accounted for by propagating the local state estimate to the estimated epoch of the relevant measurement. For local measurements, this is determined by the observer's onboard clock. For remote measurements, this is the received time-tag plus the estimated differential clock offset for that observer.

5. OBSERVABILITY ANALYSIS

The problem of simultaneously estimating the absolute orbit of an observer and relative orbit of a target with angles-only measurements has been recently examined in [19], demonstrating that the complete swarm state is not observable for a single observer and target. Additionally, [15] suggests that under some conditions, three-spacecraft swarms are weakly observable with bearing angles. However, both studies only apply single observer/target pairs – to investigate the general feasibility of ARTMS, it is useful to extend these analyses to multiple swarm observers in Mars orbit for a quantitative indication of which state components can be estimated to useful accuracy. To enable comparison with prior work, this paper applies a similar methodology to [19]. A state covariance matrix is computed from a measurement sensitivity matrix and measurement noise matrix, which is used to determine the precision to which state components can be estimated.

Numerical Observability Model

Consider a model providing inertial bearing angle measurements $\boldsymbol{z}$ as a function of swarm state $\boldsymbol{x}$, local observer o, estimation epoch t_{est}, and measurement epoch t, of the form

$$\boldsymbol{z}(t) = h(\boldsymbol{x}, o, t_{\text{est}}, t) \tag{17}$$

Let bearing angles be provided at N epochs $t_1, ..., t_N$, collectively referred to as $\boldsymbol{t}_m$. Additionally, let there be M swarm observers $o_1, ..., o_M$, collectively referred to as $\boldsymbol{o}_s$. Define the clock error $c_{\text{err}}(o, t)$ of observer o at epoch t. Then, the batch of measurements received by a single observer from all swarm observers at specific epoch t is

$$\boldsymbol{y}_o(t) = \begin{pmatrix} h(\boldsymbol{x}, o_1, t_{\text{est}}, t + c_{\text{err}}(o_1, t)) \\ \vdots \\ h(\boldsymbol{x}, o_M, t_{\text{est}}, t + c_{\text{err}}(o_M, t)) \end{pmatrix} \tag{18}$$

and across all epochs, the batch of measurements received by a single observer from all swarm observers is

$$\boldsymbol{y} = g(\boldsymbol{x}, \boldsymbol{o}_s, t_{\text{est}}, \boldsymbol{t}_m) = \begin{pmatrix} \boldsymbol{y}_o(t_1) \\ \vdots \\ \boldsymbol{y}_o(t_N) \end{pmatrix} \tag{19}$$

Here, measurements are obtained by numerical integration of the GVE for for all swarm members, as per Section 2, from t_{est} to each measurement epoch. Measurements are computed from the propagated orbits.

It is then necessary to evaluate the partial derivatives of measurements with respect to each component of $\boldsymbol{x}$, for

$$\boldsymbol{Y}_{\text{est}}(\boldsymbol{x}) = \frac{\partial g(\boldsymbol{x}, \boldsymbol{o}_s, t_{\text{est}}, \boldsymbol{t}_m)}{\partial \boldsymbol{x}_{\text{est}}}\Big|_{\boldsymbol{x}} \tag{20}$$

where $\boldsymbol{x}_{\text{est}}$ are the estimated components of $\boldsymbol{x}$. The partial derivatives for each specific measurement are computed numerically via central difference, using

$$\frac{\partial \boldsymbol{h}}{\partial x}\Big|_{\boldsymbol{x}} = \frac{\boldsymbol{h}(\boldsymbol{x} + \Delta\boldsymbol{x}, o, t_{\text{est}}, t) - \boldsymbol{h}(\boldsymbol{x} - \Delta\boldsymbol{x}, o, t_{\text{est}}, t)}{2||\Delta\boldsymbol{x}||} \tag{21}$$

where $\Delta\boldsymbol{x}$ is a vector that is zero except for the specific state component where sensitivity is being evaluated. Sizes used for the central difference are 10m for the semimajor axis, 10m/a_o for the other OE, 1m/a_o for all ROE, 0.1s for clock offset, and 10^{-5} for clock drift rate.

The observability analysis is based on the following model [19] for the relationship between the covariance matrix $\boldsymbol{R}$ for the complete measurement batch, and the covariance matrix $\boldsymbol{P}_{\text{est}}$ for the estimated state, given by

$$\boldsymbol{R} = \boldsymbol{Y}_{\text{est}}(\boldsymbol{x}) \boldsymbol{P}_{\text{est}} \boldsymbol{Y}_{\text{est}}^T(\boldsymbol{x}) \tag{22}$$

When $\boldsymbol{Y}_{\text{est}}$ is full column rank – as is the case for all scenarios here – $\boldsymbol{P}_{\text{est}}$ can be computed as

$$\boldsymbol{P}_{\text{est}} = \left(\boldsymbol{Y}_{\text{est}}^T(\boldsymbol{x}) \boldsymbol{Y}_{\text{est}}(\boldsymbol{x})\right)^{-1} \left(\boldsymbol{Y}_{\text{est}}^T(\boldsymbol{x}) \boldsymbol{R} \boldsymbol{Y}_{\text{est}}(\boldsymbol{x})\right) \times \left(\boldsymbol{Y}_{\text{est}}^T(\boldsymbol{x}) \boldsymbol{Y}_{\text{est}}(\boldsymbol{x})\right)^{-1} \tag{23}$$

An advantage of computing $\boldsymbol{P}_{\text{est}}$, compared to evaluating the Lie derivatives or observability Gramian, is that accuracy requirements can be related to specific terms of $\boldsymbol{P}_{\text{est}}$. The matrix $\boldsymbol{R}$ follows the formulation in [19], which assumes independent measurements with identical noise distributions, no uncertainty in a-priori state information, and perfect knowledge of dynamics. $\boldsymbol{P}_{\text{est}}$ thus provides an indication of a lower bound for achievable estimation accuracy. If $\boldsymbol{R}_1$ is the measurement noise matrix for a single measurement, $\boldsymbol{R}$ is

$$\boldsymbol{R} = \begin{bmatrix} \boldsymbol{R}_1 & \boldsymbol{0} & \dots & \boldsymbol{0} \\ \boldsymbol{0} & \boldsymbol{R}_1 & \dots & \boldsymbol{0} \\ \vdots & \vdots & \ddots & \vdots \\ \boldsymbol{0} & \boldsymbol{0} & \dots & \boldsymbol{R}_1 \end{bmatrix} \tag{24}$$

Below, observability of the complete swarm state is evaluated for six configurations:

1. Two swarm members, with one observer
2. Two swarm members, all observers
3. Three swarm members, with two observers
4. Three swarm members, all observers
5. Four swarm members, with two observers
6. Four swarm members, all observers

Each observer takes measurements of all other swarm spacecraft. Additionally, two different absolute orbits are explored: a near-circular low Mars orbit reminiscent of Mars Odyssey [41], and an eccentric Mars orbit reminiscent of MAVEN [42]. Two different relative orbit geometries are tested: one that provides long-term passive safety via relative eccentricity/inclination (E/I) vector separation [22], as well as an in-train (IT) formation that provides near-constant along-track separation (a common but less observable scenario). Tables 1 and 2 present the relevant OE and ROE. In these tables, the first and second swarm configurations consist of Spacecraft 1 and 2; the third and fourth configurations consist of Spacecraft 1 to 3; and the fifth and sixth consist of Spacecraft 1 to 4. In the third configuration, Spacecraft 1 and 3 are observers. In the fifth configuration, Spacecraft 1 and 4 are observers. Table 3 presents the clock errors used.

Bearing angles are assumed to be subject to 20 arcsec of 1-σ noise, with $\boldsymbol{R}_1 = 9.4e\text{-}9\boldsymbol{I}_{2x2}$. This is representative of errors from modern nanosatellite star tracker cameras [43]. Two orbits of measurements are provided, with 50 measurements per orbit at evenly-spaced intervals. Perturbations included in the system dynamics for this analysis are a 4x4 Mars GMM-3 gravity model [36], a cannonball drag model with an exponential approximation of Mars atmospheric density [44], a cannonball solar radiation pressure model with cylindrical Mars shadow, and third-body Sun gravity. The dynamics numerical integration timestep is 30s. Each spacecraft is modelled as a 12U CubeSat.

Table 1. Swarm OE and ROE for the near-circular absolute orbit and E/I-vector separated relative orbit.

OE	S/C 1	ROE	S/C 2	S/C 3	S/C 4
a (km)	3789	δa (m)	0	0	0
e	0.001	$\delta\lambda$ (km)	40	80	120
i (°)	93	δe_x (m)	0	1000	0
Ω (°)	0	δe_y (m)	2000	2000	-3000
ω (°)	0	δi_x (m)	0	1000	0
M_0 (°)	0	δi_y (m)	2000	2000	-3000

Table 2. Swarm OE and ROE for the eccentric absolute orbit and in-train relative orbit.

OE	S/C 1	ROE	S/C 2	S/C 3	S/C 4
a (km)	5720	δa (m)	0	0	0
e	0.38	$\delta\lambda$ (km)	40	80	120
i (°)	75	δe_x (m)	0	0	0
Ω (°)	0	δe_y (m)	0	0	0
ω (°)	0	δi_x (m)	0	0	0
M_0 (°)	0	δi_y (m)	0	0	0

Table 3. Swarm observer clock errors.

Clock Error	S/C 1	S/C 2	S/C 3	S/C 4
δc_{err} (s)	-0.5	-1.0	-1.5	-2.0
δd_{err} (μs/s)	-0.5	-1.0	-1.5	-2.0

Numerical Results

First, it is useful to investigate how the estimation of different state subsets affects overall observability and estimation performance. The second multi-observer configuration (three spacecraft, two observers) is used, in a near-circular orbit and E/I-vector separated formation. Four sets of state components are evaluated: 1) target ROE, 2) target ROE and differential clock offsets, 3) observer OE and target ROE, and 4) observer OE, target ROE and target differential clock offsets. The 1-σ uncertainty for each subset is provided in Table 4, computed via the square root of the corresponding element on the main diagonal of $\boldsymbol{P}_{\text{est}}$. If a state component is not part of the subset, it is denoted by '-' in the corresponding column. When appropriate, uncertainties are scaled by the semimajor axis to provide a geometric interpretation of accuracy. Quantities denoted by a bar indicate a mean uncertainty averaged across all swarm observers and their tracked targets.

Several conclusions can be drawn. First, estimating differential clock offsets and drift rates has little effect on the accuracy of absolute and relative state estimates. This is evidenced by the very minor differences in accuracy between Columns 1 and 2, or Columns 3 and 4. Second, the addition of absolute state estimation does diminish the accuracy of relative state estimation. For example, uncertainty in $\delta\lambda$ is three times larger in Column 4 compared to Column 2. However, in contrast to prior work that investigated single observers only [19], it is apparent that the complete swarm state can be reasonably estimated using multiple observers.

Table 5 explores observability for different swarm configurations. The complete swarm state is estimated for the near-circular orbit and E/I-vector separated formation. In Columns 1 and 2, there exists very large uncertainties in $\sigma_u, \sigma_{\delta\lambda}, \sigma_{\delta e_y}$ and $\sigma_{\delta i_y}$, i.e. Swarms 1 and 2 are unable to estimate the complete state. Although Swarm 2 contains two observers, they both measure equivalent but 'mirrored' bearing angles, which does not provide additional geometric information that could improve observability or distinguish unobservable modes. However, in Columns 3 and 4, the maximum uncertainties are less than 1 km and the complete state becomes observable once a third spacecraft is added. This introduces an additional reference point that makes changes in the absolute and relative orbits geometrically unique, with respect to changes in bearing angles. Observability further improves in Columns 5 and 6 when adding more spacecraft and more observers to the swarm. However, the accuracy of clock estimation does slightly worsen with more observers because more clock errors must be taken into account.

Table 4. Uncertainties for subsets of estimated states: three spacecraft, two observers, in a near-circular Mars orbit and an E/I-vector separated formation.

Subset	$\delta\boldsymbol{\alpha}$	$\delta\boldsymbol{\alpha}, \delta\boldsymbol{c}_{\text{err}}$	$\boldsymbol{\alpha}, \delta\boldsymbol{\alpha}$	$\boldsymbol{\alpha}, \delta\boldsymbol{\alpha}, \delta\boldsymbol{c}_{\text{err}}$
$\overline{\sigma_a}$ (m)	-	-	4.3	5.6
$a\overline{\sigma_{e_x}}$ (km)	-	-	0.23	0.23
$a\overline{\sigma_{e_y}}$ (km)	-	-	0.26	0.26
$a\overline{\sigma_i}$ (km)	-	-	0.54	0.54
$a\overline{\sigma_\Omega}$ (km)	-	-	0.66	0.66
$a\overline{\sigma_u}$ (km)	-	-	0.32	0.33
$a\overline{\sigma_{\delta a}}$ (m)	1.3	1.3	2.2	2.2
$a\overline{\sigma_{\delta\lambda}}$ (km)	0.15	0.16	0.44	0.45
$a\overline{\sigma_{\delta e_x}}$ (m)	2.0	2.1	6.9	7.0
$a\overline{\sigma_{\delta e_y}}$ (m)	4.1	4.3	11.9	12.1
$a\overline{\sigma_{\delta i_x}}$ (m)	2.0	1.2	11.6	11.6
$a\overline{\sigma_{\delta i_y}}$ (m)	4.1	4.3	14.3	14.4
$\overline{\sigma_{\delta c_{err}}}$ (ms)	-	11	-	13
$\overline{\sigma_{\delta d_{err}}}$ (μs/s)	-	1.0	-	1.3

Table 6 presents observability results for different absolute and relative orbits. The complete state is estimated using the four-spacecraft swarm with two observers. In Column 2, the in-train formation sees noticeably diminished observability, partly due to the difficulty of distinguishing δa and $\delta\lambda$ from bearing angles. Nevertheless, reasonable accuracy remains achievable because multiple observers provide stereo measurements with which to determine target range. The eccentric orbit in Columns 3 and 4 improves observability for both formation types, and in particular benefits the in-train formation compared to Column 2. Orbit eccentricity introduces nonlinearities in the bearing angle measurements which improve overall observability.

The above analysis suggests that complete swarm states are observable using angles-only measurements, provided that multiple observers and at least three spacecraft are present. This provides useful guidelines as to when angles-only navigation is feasible and what level of accuracy can be potentially achieved. In ideal cases, using a four-spacecraft swarm, it may be possible to determine the absolute orbit to within 500m and relative orbits to within 0.2% of target range, after two orbits. In general, the least observable state components are $\delta\lambda, \Omega$ and u, while conversely, a and the other ROE can

Table 5. Uncertainties for different swarm configurations: estimating the complete swarm state in a near-circular Mars orbit and an E/I-vector separated formation.

# Members	2	2	3	3	4	4
# Observers	1	2	2	3	2	4
$\overline{\sigma_a}$ (m)	318	220	5.6	5.2	4.2	4.1
$a\overline{\sigma_{e_x}}$ (km)	4.7	3.3	0.23	0.18	0.10	0.07
$a\overline{\sigma_{e_y}}$ (km)	375	265	0.26	0.20	0.13	0.08
$a\overline{\sigma_i}$ (km)	5.0	3.5	0.54	0.41	0.22	0.16
$a\overline{\sigma_\Omega}$ (km)	376	265	0.66	0.50	0.46	0.29
$a\overline{\sigma_u}$ (km)	7530	5300	0.33	0.20	0.14	0.09
$a\overline{\sigma_{\delta a}}$ (m)	1.6	1.1	2.2	1.6	1.4	0.9
$a\overline{\sigma_{\delta\lambda}}$ (km)	1.5e4	1.1e4	0.45	0.29	0.15	0.08
$a\overline{\sigma_{\delta e_x}}$ (m)	5.0	3.6	7.0	4.7	3.1	1.9
$a\overline{\sigma_{\delta e_y}}$ (m)	7.5e5	5.3e5	12.1	8.0	7.0	4.1
$a\overline{\sigma_{\delta i_x}}$ (m)	16.7	11.8	11.6	7.9	9.7	5.1
$a\overline{\sigma_{\delta i_y}}$ (m)	7.5e5	5.3e5	14.4	9.7	8.3	4.9
$\overline{\sigma_{\delta c_{err}}}$ (ms)	-	31	12	23	7.3	19
$\overline{\sigma_{\delta d_{err}}}$ (μs/s)	-	3.7	1.4	2.7	0.8	2.2

Table 6. Uncertainties for different swarm orbits, when estimating the complete swarm state with four swarm members and two observers.

Orbit and Formation	Circ. E/I	Circ. IT	Eccen. E/I	Eccen. IT
$\overline{\sigma_a}$ (m)	4.2	17	5.5	6.6
$a\overline{\sigma_{e_x}}$ (km)	0.10	3.0	0.05	0.05
$a\overline{\sigma_{e_y}}$ (km)	0.13	2.9	0.05	0.34
$a\overline{\sigma_i}$ (km)	0.22	2.5	0.06	0.07
$a\overline{\sigma_\Omega}$ (km)	0.46	2.5	0.16	0.18
$a\overline{\sigma_u}$ (km)	0.14	1.7	0.14	0.65
$a\overline{\sigma_{\delta a}}$ (m)	1.4	16	0.8	7.6
$a\overline{\sigma_{\delta\lambda}}$ (km)	0.15	2.1	0.16	0.28
$a\overline{\sigma_{\delta e_x}}$ (m)	3.1	63	1.5	4.8
$a\overline{\sigma_{\delta e_y}}$ (m)	7.0	62	6.7	0.8
$a\overline{\sigma_{\delta i_x}}$ (m)	9.7	52	2.6	2.5
$a\overline{\sigma_{\delta i_y}}$ (m)	8.3	52	6.7	0.6
$\overline{\sigma_{\delta c_{err}}}$ (ms)	7.3	9.4	12	14
$\overline{\sigma_{\delta d_{err}}}$ (μs/s)	0.8	1.1	0.7	0.8

be estimated with high precision. This matches the expected behavior of inter-satellite bearing angle measurements: range $\delta\lambda$ is weakly observable and is dependent on u and Ω, while the other ROE and resulting out-of-plane motion have much stronger effects on bearing angles.

6. MISSION SIMULATION

Proposed Mission

To validate the observability analysis and demonstrate the overall feasibility of autonomous angles-only swarm navigation, a simulation scenario is developed for a proposed Mars science mission. It presents an example of a future swarm mission enabled by angles-only navigation techniques. The swarm consists of four 12U CubeSats which take distributed measurements of the Martian atmosphere, thermosphere, ionospheric plasmas, and transient magnetic fields. By doing so, better understanding of Martian weather, atmospheric structure and ionospheric interactions can be achieved. These objectives are partly inspired by past missions such as NASA's MAVEN spacecraft, which studies the atmosphere and ionosphere of Mars to provide insight into how the planet's climate has changed over time [42]. Another inspiration is the upcoming SWARM-EX mission, which will use multiple cooperative CubeSats to measure ionized and neutral gases in Earth's upper atmosphere [7]. It applies a distributed measurement framework to observe atmospheric structure with varying temporal and spatial resolutions, otherwise impossible with a single spacecraft. However, SWARM-EX is Earth-orbiting and will navigate with GNSS. In contrast, the proposed Mars swarm must navigate using bearing angles exclusively. Crucially, the objective of distributed atmospheric measurements does not require extremely precise swarm positioning knowledge. The mission can therefore be carried out using angles-only as the sole navigation method.

It is proposed that the swarm is carried to Mars aboard a larger, primary spacecraft, and is deployed upon insertion into Mars orbit. The swarm initially deploys into a simple in-train formation, whereupon it commences angles-only navigation. The swarm then reconfigures into a nominal science formation with E/I-vector separation between members. Over the course of the mission, the swarm executes regular planned reconfigurations (e.g. monthly) to achieve varying measurement baselines. Measurement data is broadcast to the primary spacecraft when in suitable proximity, which the primary spacecraft then relays to Earth. This is considered feasible as the science objective does not require particularly high data volumes. The only necessary ground contacts from a navigation perspective are telecommands to provide required ARTMS inputs, such as the single DSN absolute orbit and clock initialization for each swarm observer, planned maneuvers, and specific algorithm parameters.

For simulation, the absolute orbit of the swarm is based on the 2020 orbit of MAVEN [42]. The orbit is eccentric with a period of approximately 3.5 hours, perigee altitude of 150 km, and apogee altitude of 4500 km. OE and ROE for a representative science formation are given in Table 7. OE and ROE during deployment are given in Table 8. ROE are computed relative to Spacecraft 1. Spacecraft 1 and 4 are designated as observers, while other swarm members conduct science activity but do not actively run ARTMS. To enable consistent swarm observation, it is assumed Spacecraft 1 maintains its attitude such that its camera boresight is consistently aligned with its local $\hat{\boldsymbol{y}}^{\mathcal{W}}$ direction (i.e. the instantaneous velocity direction). Spacecraft 4 points its camera boresight in $-\hat{\boldsymbol{y}}^{\mathcal{W}}$.

Table 7. Swarm configuration for mission science operations.

OE	S/C 1	ROE	S/C 2	S/C 3	S/C 4
a (km)	5720	δa (m)	-2	2	3
e	0.38	$\delta\lambda$ (km)	20	40	60
i ($^\circ$)	75	δe_x (m)	300	600	-800
Ω ($^\circ$)	0	δe_y (m)	300	600	-800
ω ($^\circ$)	0	δi_x (m)	200	-400	800
M_0 ($^\circ$)	180	δi_y (m)	200	-400	800

Table 8. Swarm configuration for mission deployment operations.

OE	S/C 1	ROE	S/C 2	S/C 3	S/C 4
a (km)	5720	δa (m)	-2	2	3
e	0.38	$\delta\lambda$ (km)	50	100	150
i (°)	75	δe_x (m)	30	40	40
Ω (°)	90	δe_y (m)	40	-40	40
ω (°)	90	δi_x (m)	30	-30	-30
M_0 (°)	0	δi_y (m)	30	-30	-30

Figure 9 visualizes the absolute orbit of Spacecraft 1 around Mars for the science formation. In this configuration, significant eclipse periods (yellow) and sun-blinding periods (red) are present for the onboard VBS. Approximately 50% of the orbit cannot supply angles-only measurements, presenting a challenging scenario for navigation. Figures 10 and 11 present target relative orbits, with respect to Spacecraft 1, for the science and deployment formation respectively.

A reconfiguration scenario is also defined. For this, the swarm begins in the deployment configuration but with modified OE of $\Omega = 22.5°$and $\omega = 45°$. Three maneuvers are performed by Spacecraft 1. First is a cross-track maneuver with magnitude 0.3 m/s at time $t = 5$ hours, to introduce out-of-plane relative motion. Second is an along-track maneuver with magnitude 0.2 m/s at time $t = 10$ hours, to introduce a difference in semi-major axis such that separation from targets increases over time. Third is an along-track maneuver with magnitude -0.2 m/s at time $t = 20$ hours, to remove the difference in semi-major axis and recover bounded relative orbits. The combined effect of these maneuvers is to reconfigure into a science formation with larger target ranges of $\delta\lambda = (100, 150, 200)$ km with respect to Spacecraft 1. Figure 12 presents the motion of Spacecraft 2, 3, and 4 relative to local observer Spacecraft 1.

Data Generation

Generation of simulation data consists of four steps: 1) simulation of ground truth, 2) synthesis of noisy input measurements, 3) collection of HIL measurements, and 4) collection of ARTMS telemetry.

Ground truth positions and velocities of the four-spacecraft swarm are numerically integrated using Stanford SLAB's

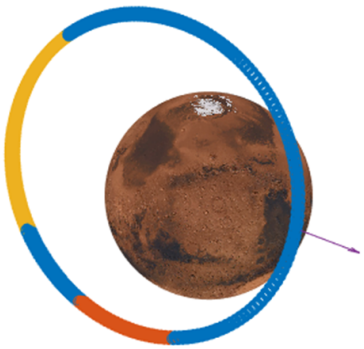

Figure 9. Absolute orbit of Spacecraft 1 during science operations. Eclipses are in yellow and sun-blinding periods are in red. The purple vector indicates sun direction.

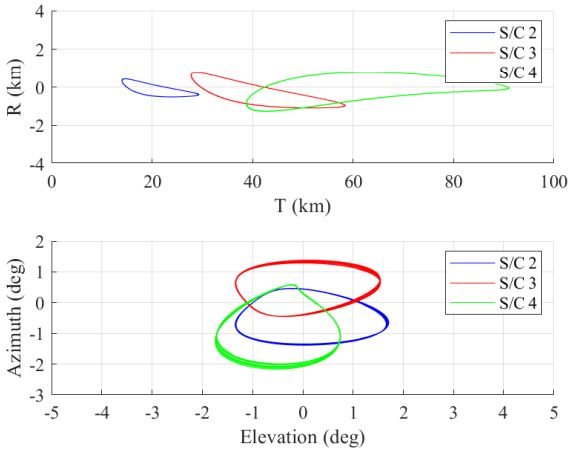

Figure 10. Science formation. Relative positions of S/C 2, 3, 4 with respect to S/C 1 in the RT plane (top) and RN plane or image plane (bottom).

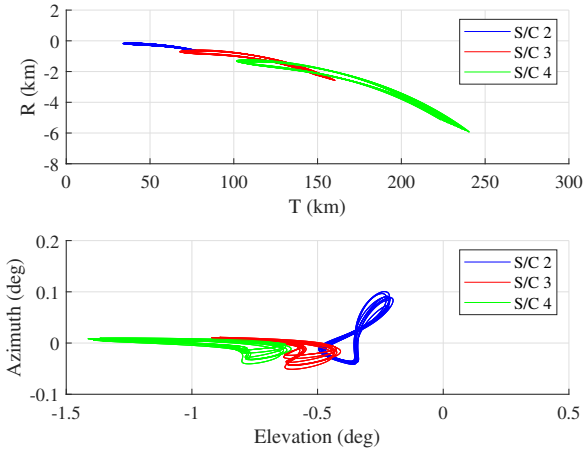

Figure 11. Deployment formation. Relative positions of S/C 2, 3, 4 with respect to S/C 1 in the RT plane (top) and RN plane or image plane (bottom).

S^3 software [45], with the addition of new models adapted for the Mars dynamic environment. Included perturbations are a 60x60 Mars GMM-3 gravity model [36], a cannonball drag model with an exponential approximation of Mars atmospheric density [44], a cannonball solar radiation pressure model with cylindrical Mars shadow, and third-body Sun gravity. Each spacecraft is modelled as a 12U CubeSat that always has its VBS aligned in the local $\pm\hat{\boldsymbol{y}}^{\mathcal{W}}$ direction. Target visibility and visual magnitudes are computed using a model from Cognion [46] which takes into account the observer-target-Sun phase angle, flux contributions from Mars albedo, and variations in reflected flux from different satellite surfaces. The nominal satellite ballistic coefficient is 0.01 with ground truth values of ± 0.002. Ground truth clocks and clock noise are propagated using the Galleani model with includes both frequency and phase noise [47]. Clock quality emulates the Microsemi SA.45s chipscale atomic clock with an Allan deviation of 10^{-10} for $\tau = 1$ second [48]. Noise values of $q_1 = (3 \times 10^{-10})^2$ and $q_2 = (3 \times 10^{-14})^2$ are applied in the clock model. In simulations, the initial differential clock offset between Spacecraft 1 and 4 is 1.5 s with an

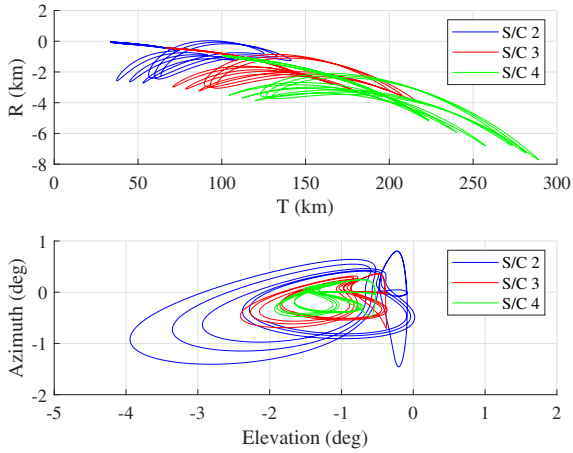

Figure 12. Swarm reconfiguration. Relative positions of S/C 2, 3, 4 with respect to S/C 1 in the RT plane (top) and RN plane or image plane (bottom).

initial differential drift rate of 1.5 μs/s. Observer maneuver knowledge possesses a 1-σ error of 5% in magnitude.

Measurements are then synthesized from ground truth. The DSN absolute orbit initalization uses a 1-σ error of 10m in position and 10 mm/s in velocity [49]. Image measurements for the local swarm observer are generated using 3D vector graphics in OpenGL [50]. The visual magnitudes, angles, and proper motions of stars are obtained from the Hipparcos star catalog and any objects within the camera FOV are rendered using Gaussian point spread functions. Noise is added to the image attitude with 6" off-axis jitter and 30" boresight jitter (1-σ). ISL measurements from remote observers are computed using 1-σ bearing angle noise of (20", 20") and attitude rotation angle noise of (6", 6", 30"). These values are considered typical for modern CubeSat star trackers and image centroiding algorithms [31] [43].

Simulations also include a CubeSat star tracker in the loop. Input images for each observer are retrieved from a Blue Canyon Technologies Nano Star Tracker as stimulated by the Stanford SLAB Optical Stimulator (OS). The OS is a a variable-magnification testbed consisting of two lenses and a microdisplay. Synthetic space scenes are generated and shown on the display. By moving the two lenses and display relative to each other, the VBS under test is stimulated with appropriate magnification. The OS is calibrated such that the VBS image is similar in both radiosity and geometry to what would be observed in orbit. Development, calibration and usage of the OS is detailed in [50] with achievable errors between desired and measured bearing angles of less than 20". Figure 13 presents the OS hardware.

After generation, all input data is sent to ARTMS for processing, which exists in a flight-code-like implementation in C++ and MATLAB Simulink. Simulations were run on a PC with an Intel i-7700HQ CPU and 16GB of RAM. The only perturbations modeled within the SOD filter are 20x20 GMM-3 spherical harmonic gravity. The SOD dynamics integration timestep is 30s. In these simulations, covariance matching techniques and empirical acceleration estimation are not applied. The initial absolute orbit estimate and covariance are provided from DSN, and the initial clock offset and drift rate estimates are zero with covariances of 1s and

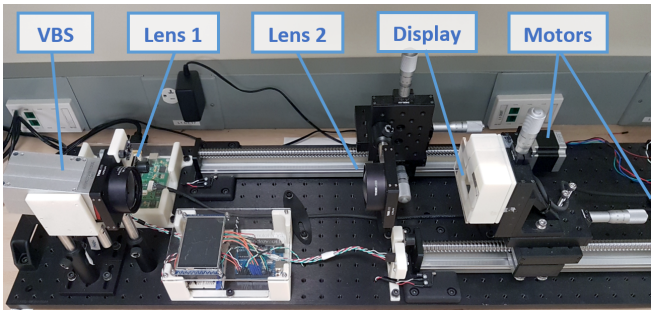

Figure 13. The SLAB Optical Stimulator.

100 μs/s respectively. No a-priori relative orbit information is provided. BOD state initialization occurs after 4 hours, upon which SOD commences refinement of orbit estimates. Image measurements are received every two minutes.

Simulation Results

Navigation results for the science formation are presented in Figures 14 and 15. Plots display position and velocity errors in the RTN frame. Time $t = 0$ in each plot corresponds to the commencement of navigation by SOD. Despite significant measurement gaps, ARTMS is able to perform both absolute and relative orbit determination. Bearing angle measurements are used to maintain the absolute orbit initialization provided by the DSN and refine the relative orbit initialization computed by BOD. The absolute orbit is estimated to 900m position accuracy at steady state, and relative orbits are estimated to 0.5% of target range. The majority of position error occurs in the along-track direction, as it is analogous to the weakly observable target range. Other components of target motion are more observable and see correspondingly smaller error. Differential clock offsets and drift rates are also effectively estimated – despite large initial errors, offsets are estimated to within 0.02s and drift rates to within 0.4 μs/s. Convergence to steady state is achieved after approximately two orbits.

The state covariance observes periodic growth and shrinkage, partly due to eclipse periods during which measurements are unavailable and covariance increases. This behavior is also influenced by orbit eccentricity. Near periapsis, swarm velocities are faster and there is more change in swarm states between measurements. Furthermore, swarm separations are larger, meaning that filter dynamics modeling is somewhat less accurate. This results in covariance growth near periapsis and shrinkage near apoapsis. Regular spikes of relative orbit error are also observed near periapsis due to the impact of drag on swarm dynamics (which is unmodeled in the filter). It is suggested that covariance matching [21] or adaptive process noise estimation [38] could be applied to effectively treat this discrepancy without requiring additional dynamics models onboard. Error spikes are also observed in the absolute orbit estimate when exiting eclipse periods – the relatively simple onboard dynamics model leads to state propagation errors. However, these are quickly recovered, indicating good robustness. In a similar vein, the initial absolute orbit error when SOD initializes is much larger than what is supplied by the DSN, because four hours of propagation are required to collect measurements for BOD (during which SOD is not receiving measurements).

Longer trials across a 200-hour time period, but without HIL measurements, display similar performance, indicating that state estimate convergence can be maintained indefinitely

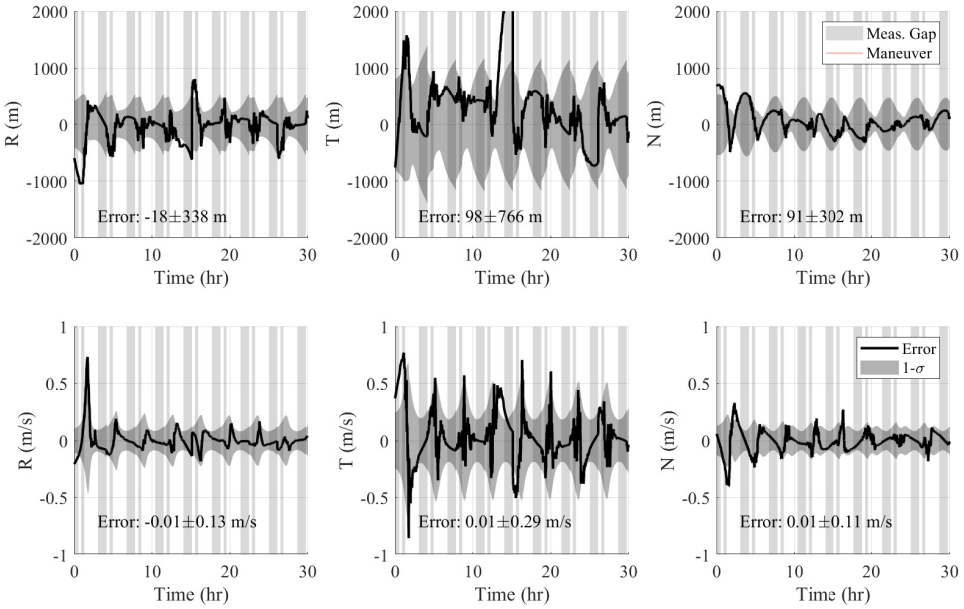

Figure 14. Absolute orbit estimation errors for Spacecraft 1 in the science formation.

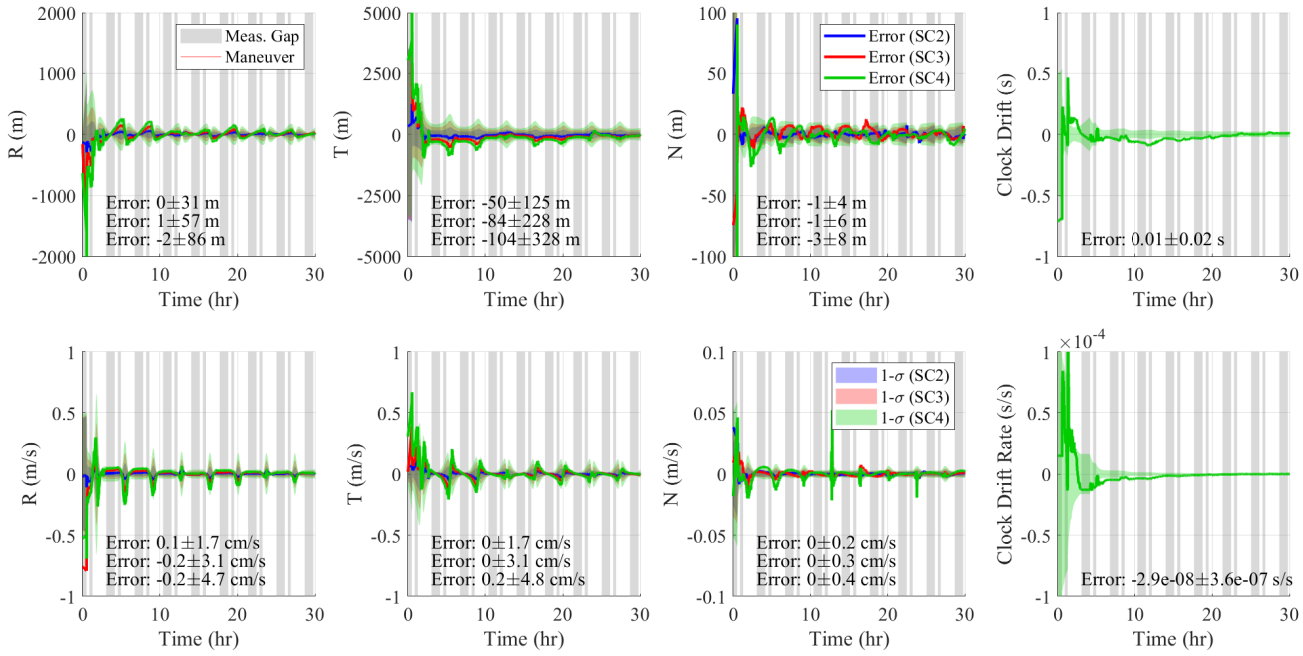

Figure 15. Relative orbit and clock offset estimation errors for Spacecraft 1 in the science formation.

with angles-only measurements. Clock error estimation is necessary to achieve this: steady-state biases of approximately 2-3% in target $\delta\lambda$ values are observed per 0.1s of differential clock offset. Divergence of the absolute orbit estimate is also observed as offsets increase, due to increasing measurement errors. At periapsis, where velocities are 3.5km/s, 0.1s of clock offset introduces roughly 350m of position error. Given that clock offset estimation is not detrimental to observability, it is strongly recommended.

Results for the deployment formation are presented in Figures 16 and 17. Despite 100% measurement availability, performance is visibly degraded compared to the previous simulation. The absolute orbit is estimated to 1200m position accuracy at steady state, and relative orbits are estimated to 0.5% of target range. Clock offsets are estimated to within 0.08s and convergence times for the relative state estimate are significantly longer. Larger error spikes are also observed in the relative state estimate near periapsis. As has been

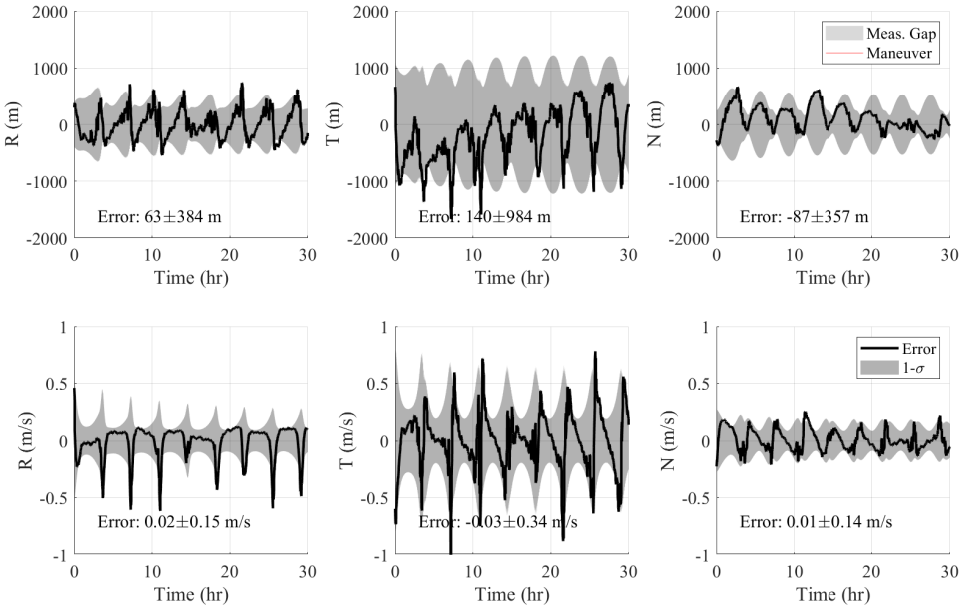

Figure 16. Absolute orbit estimation errors for Spacecraft 1 in the deployment formation.

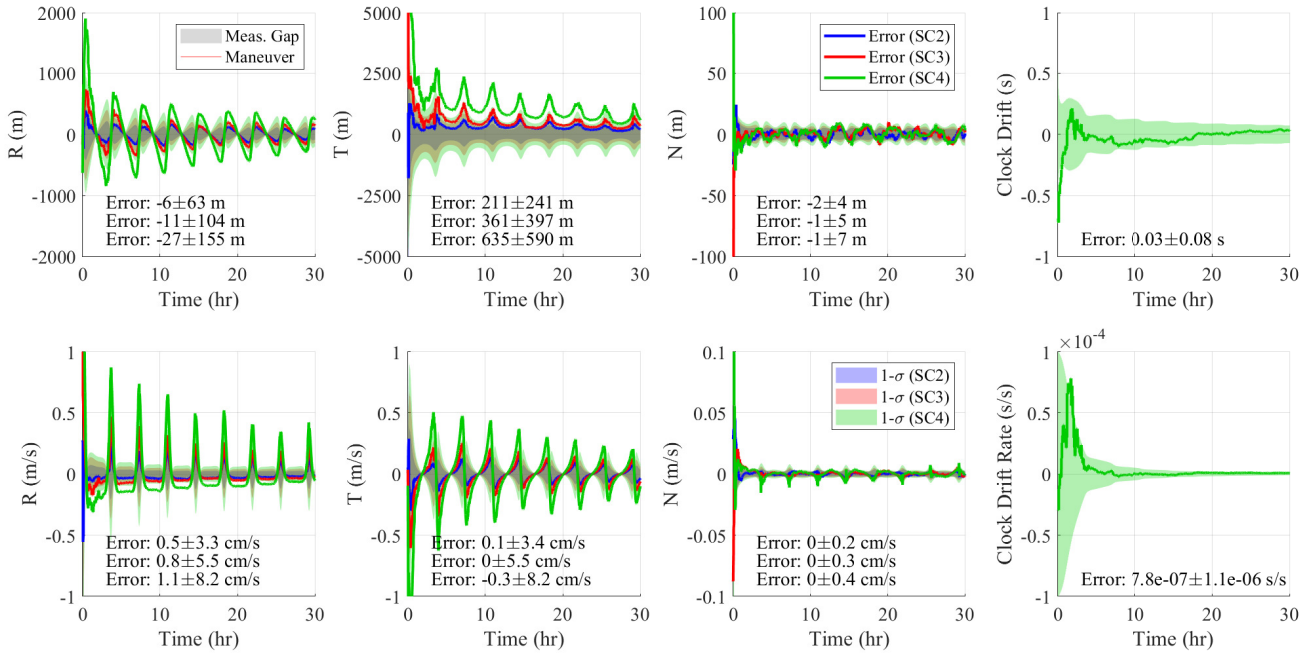

Figure 17. Relative orbit and clock offset estimation errors for Spacecraft 1 in the deployment formation.

discussed previously, in-train formations are comparatively more challenging to track, because relative motion is small and $\delta\lambda$ is only weakly observable. Nevertheless, it is still possible to achieve absolute and relative orbit determination using angles-only measurements. Two aspects act to improve observability and make this possible: first, the eccentricity of the orbit introduces additional relative motion between targets, and second, the multiple swarm observers provide improved performance via stereo measurements.

Results for the reconfiguration are presented in Figures 18 and 19. Maneuvers are provided to ARTMS via telecommands but do possess $\sim$5% magnitude errors, which leads to complications when estimating clock errors. Immediately after a maneuver, the filter is unable to distinguish whether resultant error in target positions is due to an imprecise maneuver or a change in clock offset. Sudden increases in clock estimation error are thus observed. However, the filter is able to recover clock estimates within two orbits and

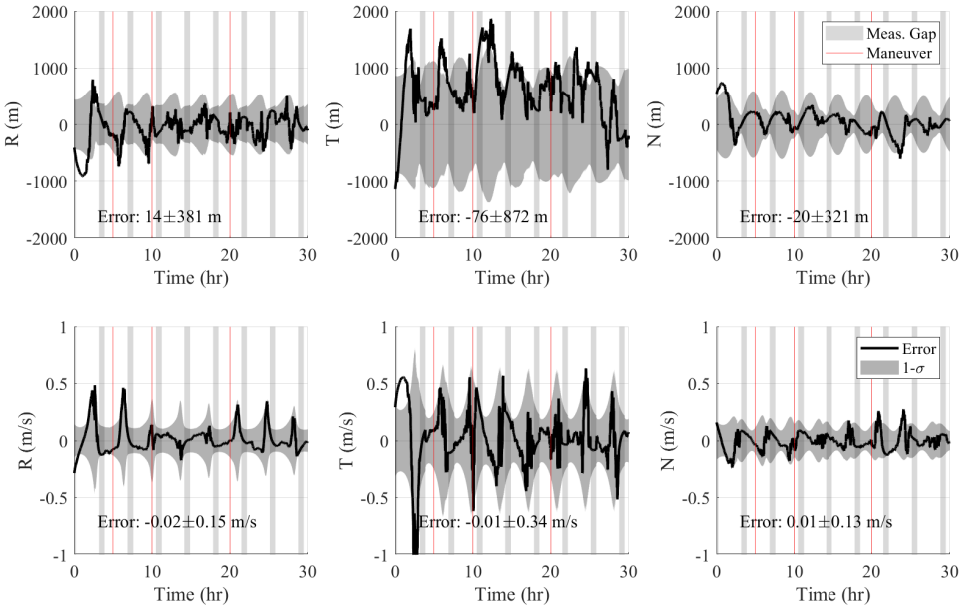

Figure 18. Absolute orbit estimation errors for Spacecraft 1 during reconfiguration.

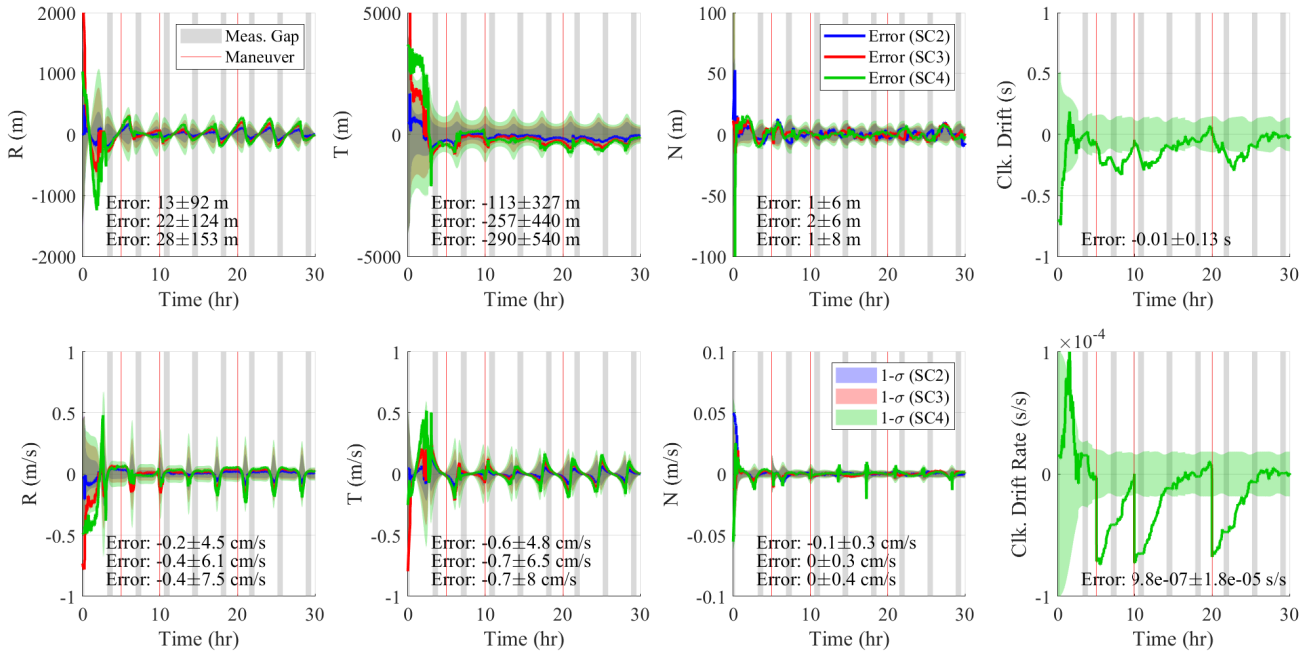

Figure 19. Relative orbit and clock offset estimation errors for Spacecraft 1 during reconfiguration.

ARTMS successfully continues orbit determination.

It is also valuable to discuss the accuracy of the ARTMS autonomous initialization. In the above trials, during initialization, IMP achieves 100% measurement assignment precision and 85% measurement assignment recall for the science formation, and 98% precision and 64% recall for deployment. During deployment, targets are in close proximity in images, and IMP elects to make no assignment if the choice is considered ambiguous. This is to ensure high precision and avoid incorrect assignments since angles-only navigation is particularly sensitive to measurement errors. Using these measurements, BOD achieves initial position errors of (1.8, 4.3, 3.8, 3.8) km for Spacecraft 1 to 4 in the deployment formation, and (1.8, 3.6, 3.5, 3) km for the science formation. As expected, these results are somewhat worse than those in the observability analysis (which applied two orbits of measurements instead of one, and assumed perfect dynamics

knowledge and better noise conditions). With the aid of subsequent measurements and the UKF, the system is able to move towards the accuracy lower bound suggested by the observability analysis.

7. CONCLUSION

This research has presented an architecture to enable autonomous navigation of spacecraft swarms in general planetary orbit regimes, by using angles-only measurements obtained by onboard cameras. Key focuses of the architecture are distribution, and treatment of arbitrary swarm configurations consisting of multiple observers and multiple targets; autonomy, via self-contained navigation in deep space with minimal ground contact; and robustness, with long-term maneuver-free convergence and sufficient accuracy to enable proposed swarm missions under realistic conditions. These goals are achieved through a novel multi-observer framework and three core algorithms. First, an image processing algorithm applies multi-hypothesis tracking and parametric models of target kinematics to produce batches of bearing angles corresponding to targets in the field of view, without a-priori target state information. Second, a batch orbit determination algorithm computes initial orbit estimates for the observer and its targets from bearing angle batches. The weakly-observable target range is estimated via sampling, and strongly-observable components are estimated using iterative batch least squares. Third, a sequential orbit determination algorithm continually refines the orbit estimates of the observer and its targets. A UKF is employed with a nonlinear dynamics model and an ROE state to resolve the weakly-observable range without requiring maneuvers. Multi-observer measurement assignment methods allow the filter to leverage measurements from both local and remote observers for greatly improved navigation performance. Clock offsets between swarm observers are also estimated on board. Together, these algorithms enable angles-only estimation of both absolute and relative swarm orbits with minimal hardware, provided that each observer receives a coarse estimate of its absolute orbit at a single epoch.

The theoretical performance of multi-observer angles-only navigation was investigated through a numerical observability analysis and computation of the estimated state covariance. Results suggest that at least three spacecraft and two observers are needed for complete swarm observability. Observability is maintained for both in-train and E/I-vector separated formations in near-circular and eccentric orbits, though in-train formations are somewhat less observable. Given two orbits of measurements and representative sensor uncertainties, the following lower bounds are computed for estimation accuracy: 500m (absolute orbit), 0.2% of target range (relative orbits) and 20 ms (differential clock offsets). This analysis is validated by camera-in-the-loop simulations of a proposed swarm science mission, consisting of four CubeSats in Mars orbit. Simulation results across different formation types demonstrate steady-state accuracies of $<$1 km in absolute position, $<$0.5% of target range in relative position, and $<$0.1 s for clock offsets. Convergence of the state estimate is maintained during long-term testing, even in the presence of significant measurement gaps and orbit perturbations. However, periodic covariance growth and estimation errors were encountered due to higher velocities and larger swarm separations near periapsis, and the effects of unmodeled dynamics in the filter. It is suggested to treat this by adding adaptive process noise estimation. Clock offset estimation is also strongly recommended to prevent large multi-observer measurement errors and state errors. Overall, simulations display promising navigation performance for a variety of swarm geometries, with sufficient accuracy to enable the proposed objective.

A key question to be addressed in future work is quantification of algorithmic complexity. Development of a flight code implementation of ARTMS is continuing, which will involve detailing of performance costs when running on CubeSat flight processors. Related aspects to be investigated are the computational scalability of ARTMS to larger swarms and choice of algorithm update timescales for improved efficiency. Flight testing of ARTMS in LEO is expected to occur in 2022 aboard the Starling technology demonstration mission under development at NASA Ames.

Further research avenues include formal definitions of swarm communication/measurement topologies and the impact of these elements on observability. Formalizing the links between swarm design and achievable navigation performance may offer insights into mission development. There is also a need to implement optimization of swarm observer attitudes, to ensure that targets remain in view for consistent observation – this may prove particularly challenging for certain swarm geometries, or if sensing is limited. Application of ARTMS to moon- or asteroid-orbiting missions characterized by weak or poorly-known gravity will also be explored.

ACKNOWLEDGMENTS

This work was supported by the NASA JPL Strategic University Research Partnership "Autonomous Deep Space Navigation using Intersatellite Optical Measurements" (2020), and by the NASA Small Spacecraft Technology Program for contribution to Starling/StarFOX efforts (cooperative agreement number 80NSSC18M0058). The authors wish to acknowledge the valuable contributions of Stefano Campagnola, Shyam Bhaskaram, Eric Gustafson and Tim McElrath of NASA JPL towards the development and outcomes of this research. The authors would also like to acknowledge the contributions of Joshua Sullivan to the development of the ARTMS architecture and algorithms, and of Toby Bell to the development of the ARTMS software modules.

REFERENCES

[1] S. D'Amico, M. Pavone, S. Saraf, A. Alhussien, T. S. Mohammed Al-Saud, S. Buchman, R. Byer, and C. Farhat, "Miniaturized Autonomous Distributed Space System for Future Science and Exploration," in *8th International Workshop on Satellite Constellations and Formation Flying*, Delft, The Netherlands, 2015.

[2] B. D. Tapley, S. Bettadpur, M. Watkins, and C. Reigber, "The Gravity Recovery and Climate Experiment: Mission Overview and Early Results," *Geophysical Research Letters*, vol. 31, no. 9, 2004.

[3] G. Krieger, A. Moreira, H. Fiedler, I. Hajnsek, M. Werner, M. Younis, and M. Zink, "TanDEM-X: A Satellite Formation for High-Resolution SAR Interferometry," *IEEE Transactions on Geoscience and Remote Sensing*, vol. 45, no. 11, pp. 3317–3341, 2007.

[4] J. Burch, T. Moore, R. Torbert, and B. Giles, "Magnetospheric multiscale overview and science objectives," *Space Science Reviews*, vol. 199, no. 1-4, pp. 5–21, 2016.

[5] S. D'Amico, "Autonomous Nanosatellite Swarming Using Radio-Frequency and Optical Navigation (ANS)," *NASA Fact Sheet, Stanford Space Rendezvous Lab (SLAB)*, 2018.

[6] H. Sanchez, D. McIntosh, H. Cannon, C. Pires, M. Field, J. Sullivan, S. D'Amico, L. Mall, and B. O'Connor, "Starling-1: Swarm Technology Demonstration," in *32nd Annual Small Satellite Conference*, Logan, UT, Aug. 2018.

[7] S. Palo, J. Thayer, and M. Pilinski, "CubeSat Ideas Lab: Space Weather Atmospheric Reconfigurable Multiscale Experiment (SWARM-EX) CubeSats," 2020.

[8] A. W. Koenig, S. D'Amico, and G. Lightsey, "Formation Flying Orbit and Control Concept for the VISORS Mission," in *AIAA Scitech 2021 Forum*, Nashville, Tennessee, 2021.

[9] S. D'Amico, J.-S. Ardaens, G. Gaias, H. Benninghoff, B. Schlepp, and J. L. Jørgensen, "Noncooperative Rendezvous Using Angles-Only Optical Navigation: System Design and Flight Results," *Journal of Guidance, Control, and Dynamics*, vol. 36, no. 6, pp. 1576–1595, Nov. 2013.

[10] G. Gaias and J.-S. Ardaens, "Flight demonstration of autonomous noncooperative rendezvous in low earth orbit," *Journal of Guidance, Control, and Dynamics*, vol. 41, no. 6, pp. 1337–1354, 2017.

[11] J.-S. Ardaens and G. Gaias, "Angles-only relative orbit determination in low earth orbit," *Advances in Space Research*, vol. 61, no. 11, pp. 2740–2760, 2018.

[12] B. Vo, M. Mallick, Y. Bar-shalom, S. Coraluppi, R. Osborne, R. Mahler, and B. Vo, "Multitarget Tracking," in *Wiley Encyclopedia of Electrical and Electronics Engineering*. Springer International Publishing, 2015.

[13] S. K. Garg, "Initial Relative Orbit Determination Using Second-Order Dynamics and Line-of-Sight Measurements," Master's thesis, Auburn University, 2015.

[14] J.-S. Ardaens and G. Gaias, "A numerical approach to the problem of angles-only initial relative orbit determination in low earth orbit," *Advances in Space Research*, vol. 63, no. 12, pp. 3884–3899, 2019.

[15] Y. Hu, I. Sharf, and L. Chen, "Three-spacecraft autonomous orbit determination and observability analysis with inertial angles-only measurements," *Acta Astronautica*, vol. 170, pp. 106–121, 2020.

[16] J. Sullivan, A. W. Koenig, J. Kruger, and S. D'Amico, "Generalized Angles-Only Navigation Architecture for Autonomous Distributed Space Systems," *Journal of Guidance, Control, and Dynamics*, 2020, submitted.

[17] A. W. Koenig, J. Kruger, and S. D'Amico, "ARTMS: Enabling Autonomous Distributed Angles-Only Orbit Estimation for Spacecraft Swarms," in *American Control Conference*, New Orleans, Louisiana, 2021.

[18] J. Kruger and S. D'Amico, "Autonomous Angles-Only Multitarget Tracking for Spacecraft Swarms," in *2020 AAS/AIAA Astrodynamics Specialist Conference*, Lake Tahoe, California, 2020.

[19] A. W. Koenig and S. D'Amico, "Observability-Aware Numerical Algorithm for Angles-Only Initial Relative Orbit Determination," in *2020 AAS/AIAA Astrodynamics Specialist Conference*, Lake Tahoe, California, 2020.

[20] D. A. Vallado and W. D. McClain, *Fundamentals of Astrodynamics and Applications*, 4th ed. Hawthorne, California: Microcosm Press, 2013.

[21] J. Sullivan and S. D'Amico, "Nonlinear Kalman Filtering for Improved Angles-Only Navigation Using Relative Orbital Elements," *Journal of Guidance, Control, and Dynamics*, pp. 1–18, Jul. 2017.

[22] S. D'Amico, "Autonomous Formation Flying in Low Earth Orbit." PhD Thesis, Delft University, 2010, oCLC: 839641932.

[23] A. W. Koenig, T. Guffanti, and S. D'Amico, "New State Transition Matrices for Relative Motion of Spacecraft Formations in Perturbed Orbits," *Journal of Guidance, Control, and Dynamics*, Sep. 2016.

[24] K. T. Alfriend, Ed., *Spacecraft Formation Flying: Dynamics, Control, and Navigation*, ser. Elsevier astrodynamics series. Oxford: Butterworth-Heinemann/Elsevier, 2010, oCLC: 699265912.

[25] D. Brouwer, "Solution of the problem of artificial satellite theory without drag," *Astronomical Journal*, vol. 64, no. 1274, pp. 378–397, 1959.

[26] R. A. Broucke, "The Effects of the J3-Harmonic (Pear Shape) on the Orbit of a Satellite," in *Predictability, Stability, and Chaos in N-Body Dynamical Systems*, A. E. Roy, Ed. New York: Plenum Press, 1991.

[27] T. Guffanti and S. D'Amico, "Linear models for spacecraft relative motion perturbed by solar radiation pressure," *Journal of Guidance, Control, and Dynamics*, pp. 1–20, 2019.

[28] M. D. Johnston, D. Tran, B. Arroyo, S. Sorensen, P. Tay, B. Carruth, A. Coffman, and M. Wallace, "Automated Scheduling for NASA's Deep Space Network," *AI Magazine*, vol. 35, no. 4, pp. 7–25, 2014.

[29] D. C. Woffinden and D. K. Geller, "Observability Criteria for Angles-Only Navigation," *IEEE Transactions on Aerospace and Electronic Systems*, vol. 45, no. 3, pp. 1194–1208, 2009.

[30] G. Gaias, S. D'Amico, and J.-S. Ardaens, "Angles-Only Navigation to a Noncooperative Satellite Using Relative Orbital Elements," *Journal of Guidance, Control, and Dynamics*, vol. 37, no. 2, pp. 439–451, Mar. 2014.

[31] T. Delabie, J. de Schutter, and B. Vandenbussche, "An Accurate and Efficient Gaussian Fit Centroiding Algorithm for Star Trackers," *Journal of the Astronautical Sciences*, vol. 61, no. 1, pp. 60–84, 2014.

[32] D. Mortari, M. A. Samaan, C. Bruccoleri, and J. L. Junkins, "The pyramid star identification technique," *Navigation*, vol. 51, no. 3, pp. 171–183, 2004.

[33] J. R. Wertz, *Spacecraft Attitude Determination and Control*. Springer Science & Business Media, 2012.

[34] S. Blackman, "Multiple hypothesis tracking for multiple target tracking," *IEEE Aerospace and Electronic Systems Magazine*, vol. 19, no. 1, pp. 5–18, 2004.

[35] M. Ester, H.-P. Kriegel, J. Sander, and X. Xu, "A Density-Based Algorithm for Discovering Clusters in Large Spatial Databases with Noise," in *Proceedings of the Second International Conference on Knowledge Discovery and Data Mining*. AAAI Press, 1996, p. 226–231.

[36] A. Genova, S. Goossens, F. G. Lemoine, E. Mazarico, G. A. Neumann, D. E. Smith, and M. T. Zuber, "Seasonal and static gravity field of Mars from MGS, Mars

Odyssey and MRO radio science," *Icarus*, vol. 272, pp. 228–245, 2016.

[37] J. Sullivan and S. D'Amico, "Adaptive Filtering for Maneuver-Free Angles-Only Navigation in Eccentric Orbits," in *27th AAS/AIAA Space Flight Mechanics Meeting*, San Antonio, Texas, 2017.

[38] N. Stacey and S. D'Amico, "Adaptive and dynamically constrained process noise estimation for orbit determination," in *2019 AAS/AIAA Astrodynamics Specialist Conference*, Portland, Maine, 2019.

[39] J. Sullivan, "Nonlinear Angles-Only Orbit Estimation for Autonomous Distributed Space Systems," Ph.D. dissertation, Stanford University, 2020.

[40] J. Sullivan, T. A. Lovell, and S. D'Amico, "Angles-Only Navigation for Autonomous On-Orbit Space Situational Awareness Applications," in *AAS/AIAA Astrodynamics Specialist Conference, Snowbird, UT*, 2018.

[41] G. B. R. Saunders, R. Arvidson *et al.*, "2001 Mars Odyssey Mission Summary," *Space Science Review*, vol. 110, pp. 1–36, 2004.

[42] J. M. G. B. M. Jakosky, R. P. Lin *et al.*, "The Mars Atmosphere and Volatile Evolution (MAVEN) Mission," *Space Science Review*, vol. 195, pp. 3–48, 2015.

[43] S. Palo, G. Stafford, and A. Hoskins, "An Agile Multi-Use Nano Star Camera for Constellation Applications," in *27th Annual AIAA/USU Conference on Small Satellites*, Logan, Utah, 2013.

[44] P. Gallais, *Atmospheric Re-Entry Vehicle Mechanics*. Berlin, Germany: Springer-Verlag Berlin Heidelberg, 2007.

[45] V. Giralo and S. D'Amico, "Development of the Stanford GNSS Navigation Testbed for Distributed Space Systems," in *Institute of Navigation, International Technical Meeting*, 2018.

[46] R. L. Cognion, "Large phase angle observations of GEO satellites," in *Sensors and Systems for Space Applications VI*, K. D. Pham, J. L. Cox, R. T. Howard, and G. Chen, Eds., vol. 8739, International Society for Optics and Photonics. SPIE, 2013, pp. 194–205.

[47] L. Galleani, L. Sacerdote, P. Tavella, and C. Zucca, "A mathematical model for the atomic clock error," *Metrologia*, vol. 40, pp. 257–264, 2003.

[48] P. Cash, W. Krzewick, P. Machado, K. R. Overstreet, M. Silveira, M. Stanczyk, D. Taylor, and X. Zhang, "Microsemi Chip Scale Atomic Clock (CSAC) technical status, applications, and future plans," in *2018 European Frequency and Time Forum (EFTF)*, Turin, Italy, 2018, pp. 65–71.

[49] J. Stauch *et al.*, "Mars Odyssey Mapping Orbit Determination," in *AAS/AIAA Astrodynamics Specialist Conference*, Big Sky, Montana, 2003.

[50] C. Beierle and S. D'Amico, "Variable magnification optical stimulator for training and validation of spaceborne vision-based navigation," *Journal of Spacecraft and Rockets*, vol. 56, no. 4, 2019.

BIOGRAPHY

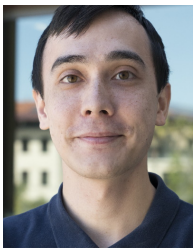

Justin Kruger *received B.S. degrees in physics and mechatronics engineering from the University of Western Australia (2016) and an M.S. degree in aeronautics and astronautics from Stanford University (2019). He is a Ph.D. candidate with the Stanford Space Rendezvous Laboratory, where his research focuses on angles-only navigation algorithms for distributed space systems in both Earth orbit and deep space. His other activities include development of an angles-only navigation software payload for the Starling1 mission being conducted by the NASA Ames Research Center, and expansion of a novel hardware-in-the-loop testbed for vision-based sensors and optical navigation algorithms. He attended the NASA Ames International Internship Program in 2018, and was joint winner of the 2018 NASA/BOEM Next Generation Animal Tracking Ideation Challenge.*

Kathryn Wallace *received a B.S.E. degree in Aerospace Engineering from the University of Michigan (2019). She is an M.S. student in Aeronautics and Astronautics at Stanford University. Her research interests include guidance and navigation for space systems.*

Adam W. Koenig *received his B.S. degree in aerospace engineering from Wichita State University in 2012 and his M.S. (2015) and Ph.D. (2019) degrees in aeronautics and astronautics from Stanford University. Dr. Koenig is currently a postdoctoral scholar in the Space Rendezvous Laboratory at Stanford University. His research interests include astrodynamics and advanced guidance, navigation, and control algorithms for distributed space systems. His current activities include development of an angles-only navigation software payload for the StarFOX experiment on the Starling1 mission in development at NASA Ames Research Center, development of the guidance, navigation, and control algorithms for the VIrtual Super-resolution Optics with Reconfigurable Swarms (VISORS) mission funded by NSF, and design and analysis of the Miniaturized Distributed Occulter/Telescope (mDOT) mission concept for direct imaging of debris disks and large planets orbiting nearby stars.*

Simone D'Amico *is Associate Professor of Aeronautics and Astronautics at Stanford University. He received B.S. and M.S. degrees from Politecnico di Milano (2003) and a Ph.D. from Delft University of Technology (2010). From 2003 to 2014, he was research scientist and team leader at the German Aerospace Center (DLR). There, he gave key contributions to the design, development, and operations of spacecraft formation-flying and rendezvous missions such as GRACE (United States/Germany), TanDEM-X (Germany), PRISMA (Sweden/Germany/France), and PROBA-3 (ESA). From 2014 to 2020 he was Assistant Professor of*

Aeronautics and Astronautics at Stanford University. He is the founding director of the Space Rendezvous Laboratory (SLAB) and Satellite Advisor of the Student Space Initiative (SSSI), Stanford's largest undergraduate organization. He has over 200 scientific publications and 3000 Google Scholar citations including conference proceedings, peer-reviewed journal articles and book chapters. Dr. D'Amico's research aims at enabling future miniature distributed space systems for unprecedented science and exploration. His efforts lie at the intersection of advanced astrodynamics, GN&C and space system engineering to meet the tight requirements posed by these novel space architectures. The most recent mission concepts developed by Dr. D'Amico are a miniaturized distributed occulter/telescope (mDOT) system for direct imaging of exozodiacal dust and exoplanets and the Autonomous Nanosatellite Swarming (ANS) mission for characterization of small celestial bodies. Dr. D'Amico's research is supported by NASA, NSF, AFRL, AFOSR, KACST, and Industry. He is Chairman of NASA's Starshade Science and Technology Working Group (TSWG); a member of the advisory board of space startup companies and VC edge funds; a member of the Space-Flight Mechanics Technical Committee of the AAS; Associate Fellow of AIAA; Associate Editor of the AIAA Journal of Guidance, Control, and Dynamics and the IEEE Transactions of Aerospace and Electronic Systems; and fellow of the NAE's US FOE Symposium. Dr. D'Amico was recipient of the Leonardo 500 Award by the Leonardo Da Vinci Society and ISSNAF (2019), the Stanford Introductory Seminar Excellence Award (2019 and 2020), the FAI/NAA's Group Diploma of Honor (2018), the Exemplary System Engineering Doctoral Dissertation Award by the International Honor Society for Systems Engineering OAA (2016), the DLR's Sabbatical/Forschungssemester in honor of scientific achievements (2012), the DLR's Wissenschaft Preis in honor of scientific achievements (2006), and the NASA Group Achievement Award for the Gravity Recovery and Climate Experiment, GRACE (2004).